Doctoral Dissertation

Research on Improving Performance of Silicon Based Anode for Lithium Ion Batteries

（リチウムイオン電池用ケイ素系負極の高性能化に関する研究）

January 2022

Yuta Kimura

Department of Chemistry and Biotechnology

Graduated School of Engineering

Tottori University

Preface

The studies presented in this thesis were carried out under the guidance of Professor Hiroki Sakaguchi, Associate Professor Hiroyuki Usui, and Associate Professor Yasuhiro Domi at Applied Chemistry Course, Department of Chemistry and Biotechnology, Graduated School of Engineering, Tottori University during 2019-2021.

The object of this thesis is to obtain new insight for improving properties of silicide/Si composite electrode for anode of lithium ion batteries and evaluate its practicality. The author wishes sincerely that the findings from this study would be able to contribute to the achievement of lithium ion batteries with high energy density.

Yuta Kimura

Department of Chemistry and Biotechnology

Graduate School of Engineering

Tottori University

4-101 Minami, Koyama-cho, Tottori 680-8552, Japan

January 2022

Content

Chapter 3

General introduction

An unprecedented revolution may begin in the automobile industry. Important technological innovations in the automotive industry may belong to following four fields: connected, autonomous, shared, and electric. Strict emission regulations have been introduced worldwide for reducing global warming. Therefore, battery electric vehicles (BEVs) have attracted increasing attention, as they do not require gasoline for power.

Lithium-ion batteries (LIBs) have the highest energy density among secondary batteries. Therefore, LIBs are widely used as power supplies for BEVs. The cruising distance of conventional BEVs is approximately 450 km. However, the cruising distance decreases under practical conditions and is not sufficient compared to the automobiles with internal combustion engines. The enhancement of the energy density of LIBs may increase the cruising distance of the BEVs.

The charge-discharge reaction of LIBs proceeds by moving Li^+ ion between the positive and negative electrodes through the electrolyte.[1,2] The change in the active materials of the positive and negative electrodes is necessary for enhancing the energy density of LIBs because the energy density of a battery is determined by the number of Li^+ ions absorbed in the positive or negative electrode. In conventional LIBs, lithium

transition metal oxides, such as $LiCoO_2$ and graphite are used as the positive and negative active materials, respectively.[3,4] The following reactions represent when $LiCoO_2$ and graphite are used:

Cathode: $LiCoO_2 \Leftrightarrow Li_{(1-x)}CoO_2 + xLi^+ + xe^-$

Anode: $C_6 + xLi^+ + xe^- \Leftrightarrow Li_xC_6$

Total: $LiCoO_2 + C_6 \Leftrightarrow Li_{(1-x)}CoO_2 + Li_xC_6$

During charging, graphite forms graphite interlayer compounds (LiC_x) by the insertion of Li^+ ions into graphene layer. Graphite is used as a conventional anode active material because its volume expansion is almost negligible during the charge-discharge cycles and it exhibits good cycle performance. However, its theoretical capacity is only 372 mAh g^{-1}. Therefore, Si, which has an extremely high theoretical capacity (3580 mAh g^{-1}) attracts much attention as a high-capacity anode active material.[5–8] Si reacts with Li^+ ions at room temperature as follows:

$Si + 3.75Li^+ + xe^- \Leftrightarrow Li_{3.75}Si$

Si produces lithium-silicon compounds (Li_xSi) during charging, and its volume expands by at most 380%. The collapse and pulverization of Si particles occur because of stress generation in the particles during the expansion and contraction. As a result, the Si particles exfoliate from the electrode causing the loss of conductive and Li^+ diffusion paths in the electrode. Moreover, continuous film formation on the new surface by the collapse of Si particles increases the electrode resistance. Therefore, Si exhibits poor cyclability.[9,10] Compositing materials that can withstand the stress generation during the charge-discharge cycles and low electrical conductivity may be used for improving the cyclic stability of Si electrodes. We reported that the following four properties were essential for compositing phases with Si:

1) Mechanical properties suitable for the relaxation of the stress from Si

2) High electrical conductivity

3) Moderate reactivity with Li^+

4) High thermodynamic stability

We reported that the cycle performance of Si electrodes improved by coating the Si surfaces with Ru, Cu, and Ni.[11–15] This was due to the relaxation of the stress generated by the coating materials during the expansion and contraction. In addition, we investigated silicide/Si composites, which consisted of Si and transition metal silicide.[16–

[19] Various silicides ($FeSi_2$/Si, $NiSi_2$/Si, VSi_2/Si, $MmSi_2$/Si, $SmSi_2$/Si, $GdSi_{1.85}$/Si, and $DySi_{1.75}$/S) were prepared, and the relationship between the properties of silicide and the electrochemical performance of silicide/Si composite electrodes was investigated. Furthermore, we studied the relationship between the electrochemical properties of silicide/Si composite electrodes and the material properties of silicides, such as indentation hardness, electrical conductivity, Li absorption capacity, and thermodynamic stability. In addition, we attempted to control the four important properties of silicide, as mentioned by compositing ternary silicides. Consequently, ternary $LaNi_xSi_{2-x}$, in which Ni partially replaced Si in $LaSi_2$, could be synthesized. The $LaNi_{0.1}Si_{1.9}$/Si electrode exhibited excellent cycling stability and high-rate performance compared to the $LaSi_2$/Si electrode.[20] Thus, our study revealed that silicide/Si composites exhibited good electrochemical properties. In our previous studies, the electrodes were fabricated using gas deposition that did not require any binder or conductive additive to analyze the fundamental properties of the silicide/Si composites.[21,22] In this study, we used a slurry electrode consisting of an active material, conductive agent, and binder to confirm the application of silicide/Si composite as an anode material for LIBs. Furthermore, we investigated a new policy for improving the properties of silicide/Si composite electrodes.

This thesis consists of the following three chapters:

Chapter 1: The arrangements between the Si and silicide phases in the silicide/Si composites are controlled by rapid quenching. The influence of the positional relationship on the anode properties of the LIBs is evaluated.

Chapter 2: The electrochemical performance of the $Cr_xV_{1-x}Si_2$/Si composite electrode is analyzed using a slurry electrode. Furthermore, the effect of silicide hardness on the cyclability of the $Cr_xV_{1-x}Si_2$/Si composite electrode is investigated by the cross-sectional observation of the electrode after charge-discharge cycles.

Chapter 3: We perform mechanical grinding (MG) treatment on the $Cr_xV_{1-x}Si_2$/Si composite to refine the structure and investigate the influence of the structural change on the electrochemical performance. In addition, the effect of additives on the electrolyte upon improving the cycle performance is analyzed.

Finally, concluding remarks are presented.

Chapter 1

Lithiation and Delithiation Properties of Silicide/Si Composite Alloy Electrodes Prepared by Rapid Quenching Method

1.1 Introduction

Silicon (Si) is very attractive as a high capacity active material for negative electrode in lithium-ion batteries (LIBs) because of its theoretical capacity value of 3580 mA h g^{-1} ($Li_{15}Si_4$).[3,6,23] However, Si expands and contracts largely during lithiation (charge) and delithiation (discharge), respectively.[24] The expansion ratio per Si atom corresponds to 380%, which generates high stress and large strain in the active materials. The strain that accumulate during repeated charge–discharge cycling causes collapse and pulverization. Consequently, Si electrode cannot exhibit sufficient cyclic stability.

Compositing transition metal silicide and Si is one of the effective methods for improving the cyclic stability of the Si electrode.[25] We have previously reported that the following four kinds of properties are essential for compositing phases with Si:[12,16,17,20,26]

1) Mechanical properties suitable for the relaxation of the stress from Si

2) High electronic conductivity

3) Moderate reactivity with Li^+

4) High thermodynamic stability

Many studies utilizing a mechanical alloying method with planetary ball mill have been reported for preparing silicide/Si composite alloys.[25,27-29] Conversely, rapid quenching method can also be used for producing Si-alloys.[30,31] We focused on this method's control over the arrangement of Si and silicide phases, by changing the additive elements. Figure 1-1 presents a schematic illustration of the structural formation of Si-alloy by rapid quenching. While the crystallizing of Si is the initial phase from the molten Si-alloy (Figure 1-1, Pattern 1), silicide phase forms around the Si phase. In contrast, in the case of crystallizing silicide phase as the initial phase (Figure 1-1, Pattern 2), Si phase forms around the silicide phase. Formation of Pattern 1 or Pattern 2 is dependent on the elements and the amount of the additives present. In this study, we prepared various binary Si-alloys and evaluated the influence of the arrangements between the Si phase and silicide phase on the anode properties of LIBs.

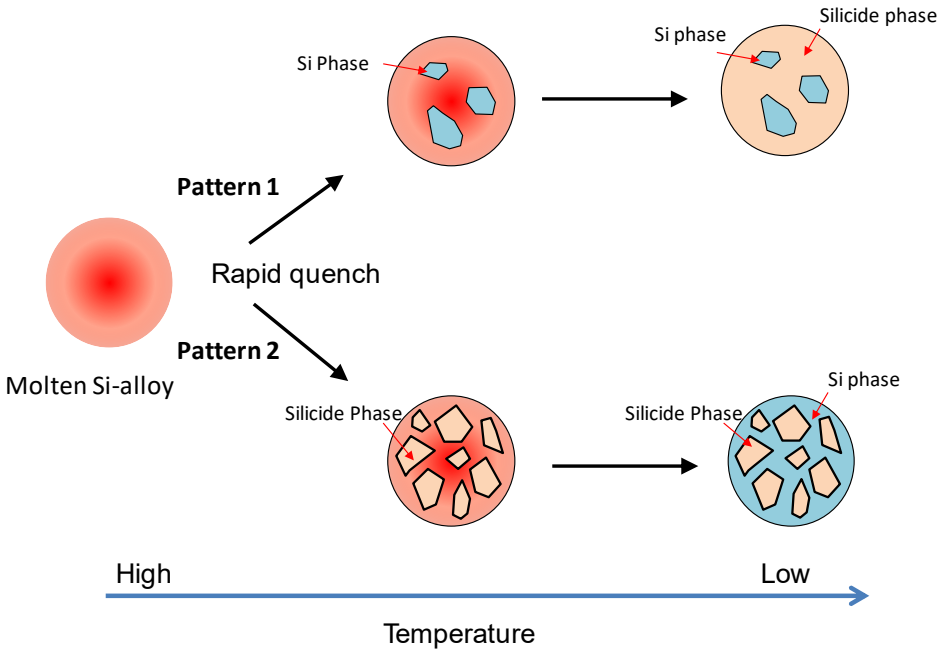

Figure 1-1. Schematic illustration of the phase-structure formation by rapid quenching method.

1.2 Experimental

1.2.1 Selection of additive element

Iron (Fe), Copper (Cu), and Cobalt (Co) were selected as the additives for making Si in the initial phase (Pattern 1) with reference to binary phase diagrams. Further, Zirconium (Zr) and Titanium (Ti) were selected for making silicide in the initial phase (Pattern 2). The corresponding amount of additives was determined by the ratio of the Si phase to silicide phase as 33:67 mass%. Table 1-1 lists the contents and the silicide phase of synthesized Si-alloys.

Table 1-1. Contents and silicide phase of synthesized Si-alloys.

Alloy type	Silicide phase	Contents (mass%)		Phase ratio (mass%)		Initial phase
		Si	X	Si	Silicide	
Si-Fe	[$FeSi_2$]	66.5	33.5	33	67	[Si]
Si-Cu	[Cu_3Si]	41.0	59.0			[Si]
Si-Co	[$CoSi_2$]	65.8	34.2			[Si]
Si-Zr	[$ZrSi_2$]	58.6	41.4			[$ZrSi_2$]
Si-Ti	[$TiSi_2$]	69.2	30.8			[$TiSi_2$]

1.2.2 Preparation of Si-alloy ribbon by rapid quenching

Si-alloys were prepared by rapid quenching. First, Si–alloy ingots were prepared in a button arc furnace. Next, the ingot was melted at approximately 1773 K in an induction furnace. After melting, the molten Si-alloy was dropped on a Cu roll at a rotating speed of 40 m/s. The molten Si-alloy was thus quenched and Si-alloy ribbons were prepared. The thickness of these ribbons was approximately 20 μm.

1.2.3 Cross-sectional observation and FE-EPMA analysis of Si-alloy ribbons

Si-alloy ribbons were placed in a Bakelite resin. Samples for the cross-sectional observation were prepared using mechanical polishing. The cross-sectional observation was performed using a scanning electron microscope (FE-SEM, SU6600, Hitachi High-Technologies Corporation). The accelerating voltage was set at 15 kV and the

magnification was 5000×. Field emission-electron probe microanalysis (FE-EPMA, JXA-8500F, JEOL, Co., Ltd.) was used for detecting the position of Si and additive elements. The accelerating voltage was 15 kV, irradiation current was 50 nA, and magnification was 5000×.

1.2.4 Cell Assembly and electrochemical measurement

Si-alloys were pulverized by hand milling and classified as <25 μm. Active material (Si-alloy powders), conductive agent (Ketjen black), and polyamic acid binder (Dreambond, I. S. T. Corporation) were mixed in the ratio of 85:5:10 (mass%). The mixture was diluted using 1-methyl-2-pyrrolidone for preparing slurry. We painted the slurry on a SUS316L foil (thickness: 20 μm) using a doctor blade with a thickness of 50 μm. SUS316L foil was used as current collector to suppress deformation during charge-discharge cycle. The electrode was then dried at 343 K for >30 min. We heated the electrode in vacuum at 573 K for 1 h for polyimidation. The electrode thickness after heating was approximately 30 μm.

A 2032-type coin cell was used for evaluating the electrochemical performance of the Si-alloy electrode. The coin cell comprised of a Si-alloy electrode as its working electrode, a glass fiber filter as the separator, and a Li metal sheet (thickness: 1 mm, diameter: 12

mm) as the counter electrode. 1 M lithium hexafluorophosphate ($LiPF_6$) dissolved in ethylene carbonate (EC): diethyl carbonate (DEC) (EC: DEC = 1:1 vol%) was employed as the electrolyte. The cell was assembled in an open dry chamber (HWR-60AR, DAIKIN INDUSTRIES Ltd.) maintaining its dew point at < –70 °C.

The charge–discharge cycle test was performed with an electrochemical measurement system (TOSCAT3100, TOYO SYSTEM Co., LTD.) in the potential range of 0.002–1.000 V vs Li^+/Li at 298 K. The current was set at 0.2 mA in the first cycle to measure accurate initial discharge capacity. After the second cycle, the current density was set to about 0.3 A g (Si+silicide) $^{-1}$.

1.3 Results and discussion

1.3.1 Characterization

We confirmed that the Si-alloys composed only of Si and silicide phases using X-ray diffraction (XRD) technique. Figure 1-2 shows the FE-EPMA analysis results of the cross-section of Si-Fe alloy and Si-Zr alloy ribbons. The elemental mapping result (Figure 1-2 (a)) confirmed that the black phase is Si and the white phase is Iron-silicide ($FeSi_2$). Hence, the silicide phase surrounded the Si phase in Si-Fe alloy. Furthermore, the black phase formed around the white phase in Si-Zr alloy (Figure 1-2 (b)), that is, Si-Zr alloy

is that Si phase surrounded silicide phase ($ZrSi_2$).

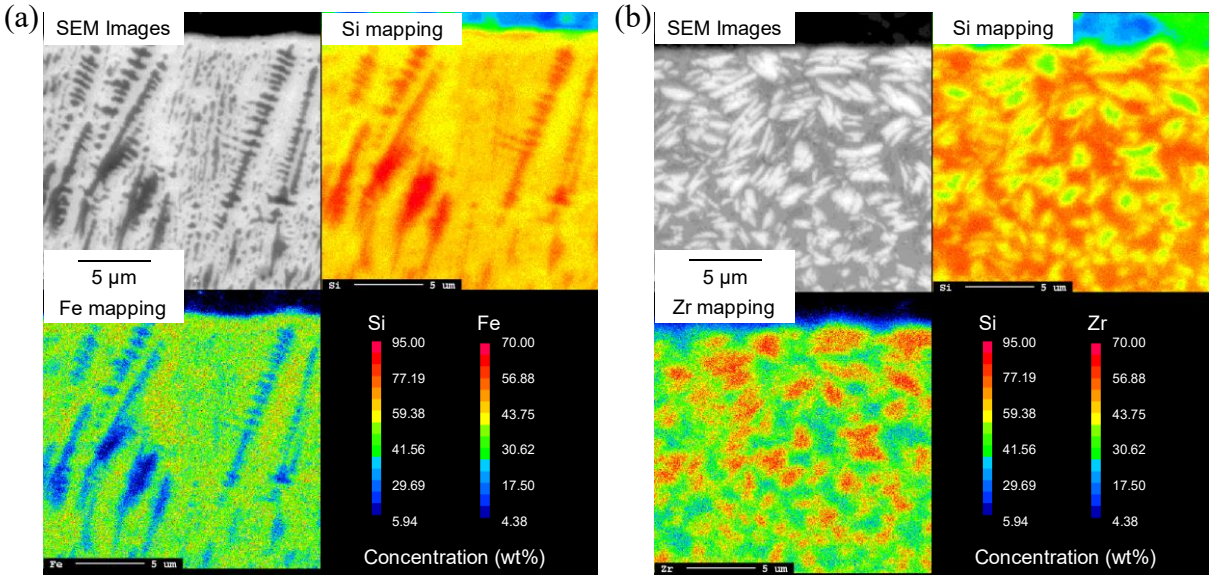

Figure 1-2. Results of FE-EPMA of prepared (a)Si-Fe alloy and (b)Si-Zr alloy on a 5 μm scale bar.

Figure 1-3 shows the cross-sectional SEM images of Si-alloy ribbons. From the positional relation of black phase (Si phase) and white phase (silicide phase) of Si-Fe, Si-Cu and Si-Co alloys, we can see that Si crystallized as the initial phase and silicide phase formed around the Si phase. For Si-Zr and Si-Ti alloys, silicide phase crystallized as the initial phase and Si phase formed around the silicide phase. Thus, by varying the additives, we could prepare various Si-alloys that differ in the positional relationship with respect to Si and silicide phases.

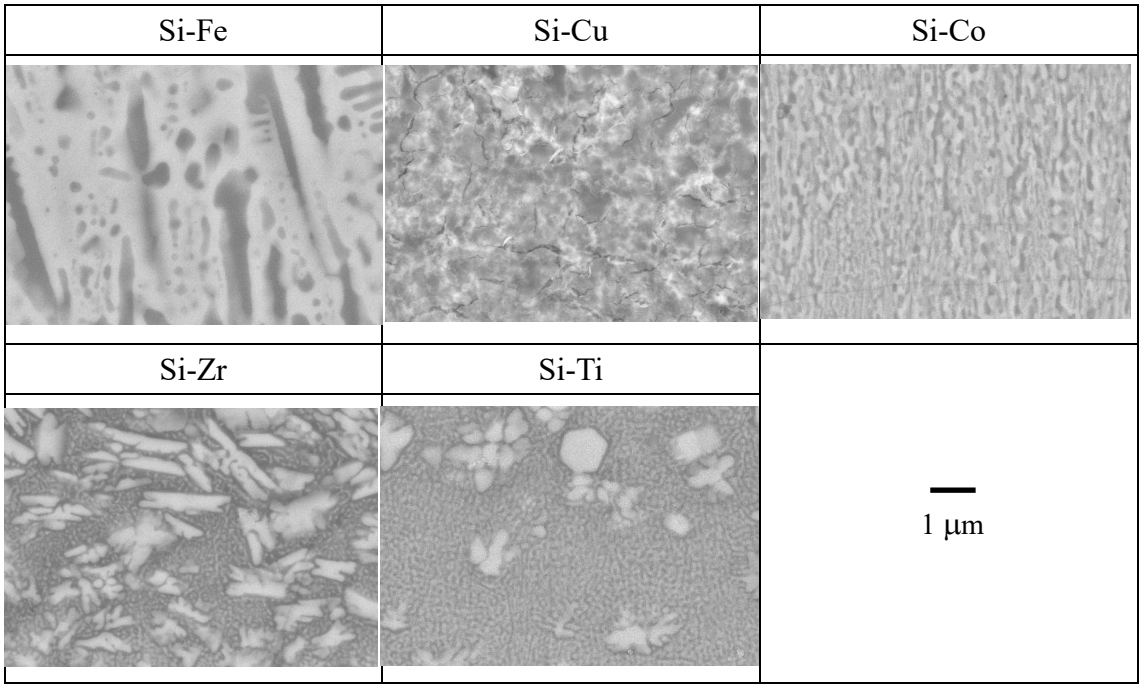

Figure 1-3. Cross-sectional SEM images of prepared Si-alloy on a 1 μm scale bar.

1.3.2 Charge–discharge cycle test of Si-alloy electrodes.

Figure 1-4 shows the results of the cycle test of Si-alloy electrodes. The discharge capacity of all Si-alloys decreased significantly during the first and second cycles. This is because of the current density in the first cycle (0.2 mA c.c., 0.075 A g $(Si+silicide)^{-1}$) is lower than that in the second cycle (0.8 mA c.c., 0.3 A g $(Si+silicide)^{-1}$) to measure the accurate initial discharge capacity of Si-alloy electrode. A decrease in the discharge capacity of Si-Fe and Si-Zr alloy electrodes from the first to second cycle was smaller than that of other Si-Cu, Si-Co, and Si-Ti electrodes, which indicates that the rate capability of the former two electrodes is superior to others. Additionally, initial discharge capacity of Si-Zr, Si-Co, and Si-Ti electrodes was higher than that of others.

After the second cycle, discharge capacity gradually decreased with a progressing cycle. We infer that the reduction of capacity is due to the gradual collapse of Si-alloy because of repeated charge-discharge and the loss of conduction path of Li-ion/electron. We can confirm that Si-Zr and Si-Ti alloy electrodes exhibit high initial capacity and good cycle stability. It is considered that four properties of silicide (electrical resistivity, reactivity with Li^+, thermodynamic stability, and mechanical properties) influence on the electrochemical performance of the silicide/Si composite electrodes.[12,16,17,20,25,26] In this study we founded that the arrangement of Si and silicide phases is likely to influence on the electrochemical performance of Si-alloy in addition to above silicide properties.

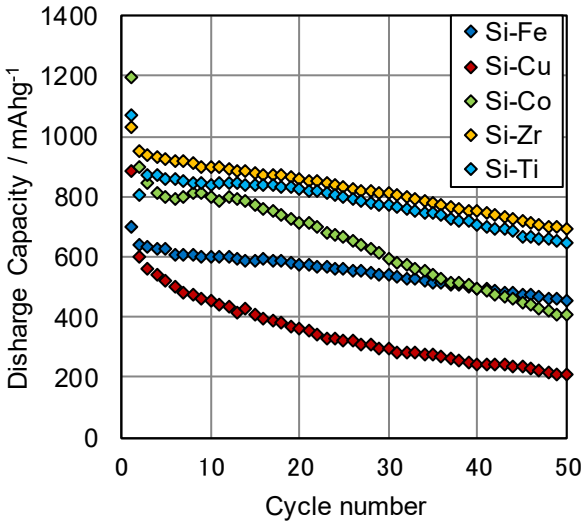

Figure 1-4. Charge–discharge cycling performances of Si-alloys.

1.3.3 Effect of the arrangement of Si and silicide phase on cycle stability.

Figure 1-5 shows the cross-sectional SEM images of Si-alloy electrodes before and after the 50th cycles. In Si-Cu and Si-Co alloys, there was a small electrode layer on the current collector because the electrode layer of those alloys reduced during rinsing of the electrode. Active material particles collapsed during the charge–discharge cycle and were exfoliated from the current collector. As the result, it was consider that the collapsed particles removed from the electrode during rinsing and the electrode layer became small. There was a space between electrode layer and current collector in Si-Cu alloy. This space may be generated during polishing for sample preparation. Further, Si-Fe alloy collapsed and was pulverized. Electrode thickness of Si-Fe alloy after the 50^{th} cycle increased by a

factor of approximately three compared to before charging. Si-Zr and Si-Ti alloys maintained their particle shape. The expanding of electrode thickness was approximately 1.5 times, which was considerably smaller than that of Si-Fe alloy. These results indicate that collapse of Si-Zr and Si-Ti alloys were suppressed during the charge–discharge cycle. We believe that the positional relation between the Si phase and the silicide phase was influential in this regard. In the Si-Fe, Si-Cu, and Si-Co alloys (Figure 1-1, Pattern 1), the silicide phase was subject to large stress due to the Li storage in the Si phase, which causes electrode expansion. As a result, Si-alloy collapsed and the electrode thickness increased. In the Si-Zr and Si-Ti alloys (Figure 1-1, Pattern 2), the stress which the silicide phase received is small because Si phase can expand outward during Li storage. Consequently, the collapse of Si-alloy particle is suppressed and the cycle stability of Si-alloy improved.

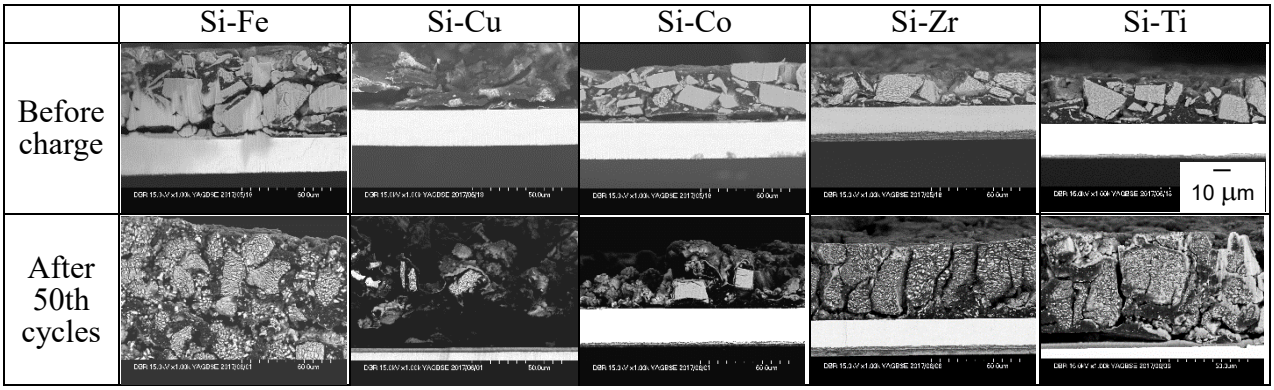

Figure 1-5. Cross-sectional SEM images of Si-alloy electrodes before and after the 50th cycle on a 10 μm scale bar.

1.4 Summary

We prepared various Si-alloys, whose structures were controlled by rapid quenching, and evaluated their electrochemical properties. Our results determined that the collapse of Si-alloy was suppressed and the cycle stability was improved by selecting additive elements (like Zr or Ti) to locate the Si phase around the silicide phase.

Chapter 2

Anode Properties of $Cr_xV_{1-x}Si_2$/Si Composite Electrodes for Lithium-ion Batteries

2.1 Introduction

The popularization of electric vehicles has resulted from the need to prevent global warming, and lithium-ion batteries (LIBs) are used in the power supplies of electric vehicles. The increase in the energy density of LIB is highly desirable because the cruising distance of conventional electric vehicles is only approximately 400 km.[1,16,17] Graphite is employed as an anode active material in LIBs; its effective capacity is approximately equal to its theoretical capacity (372 mA h g^{-1}), so any further improvement with respect to its capacity is difficult. Therefore, Si, having ten times the theoretical capacity of graphite (3580 mA h g^{-1}), is used instead. However, Si facilitates the formation of $Li_{15}Si_4$ phase, where Si absorbs Li to a large extent at room temperature, expanding by approximately 3.8 times.[18] Due to repeated charging and discharging, Si exhibits poor cyclability because Si pulverizes owing to the accumulation of strains, resulting from the change in volume.

In order to improve cyclability of Si, alloying Si and metal element such as Cu or Ni has been addressed.[19-22] We have confirmed that the cyclability can be improved by compositing transition metal silicide with Si (silicide/Si). We have also reported that the materials composted with Si require the following four properties:[5-8,23-30]

(1) Mechanical properties suitable for the relaxation of the stress from Si

(2) High electronic conductivity

(3) Moderate reactivity with Li^+

(4) High thermodynamic stability

Optimizing all the four properties together is difficult in binary silicides. Hence, we have tried to improve the properties of silicides and the anode performance of composite electrodes for LIBs by compositing ternary silicides. As a result, we have found that ternary $LaNi_xSi_{2-x}$ (AB_xSi_{y-x}-type, A and B:metal), where Ni partially replaces Si in $LaSi_2$, can be synthesized and the $LaNi_{0.1}Si_{1.9}$/Si electrode exhibits improved cycling and high-rate performances compared with the $LaSi_2$/Si electrode.[9] Furthermore, we have observed that a part of Cr is replaced by V, forming $Cr_xV_{1-x}Si_2$ ($A_{1-x}B_xSi_y$-type), when V is added to $CrSi_2$. The $Cr_{0.5}V_{0.5}Si_2$/Si electrode exhibited significantly better cycle stability than the $CrSi_2$/Si or VSi_2/Si electrodes.[31]

We have investigated the changes in the aforementioned four properties of ternary silicide. We have confirmed that property (4) is improved by replacing V, whereas properties (1) and (2) did not change. Properties (1) and (2) correspond to the parameters of elastic modulus and electrical conductivity, respectively. Property (3) is improved because of the enlargement of the crystal lattice of ternary silicide, resulting from the substitution of Cr (atomic radius:0.128 nm) by V (atomic radius:0.134 nm). Furthermore, we found that the charge repulsion between Li and the transition metal in $CrSi_2$ is smaller than the charge repulsion between Li and VSi_2, based on the result of a first-principles calculation. From the above results, it may be considered that the Li diffusion in $Cr_{0.5}V_{0.5}Si_2$ is facilitated by the following two effects:large crystal lattice of VSi_2 and small charge repulsion between Si and $CrSi_2$. As a result, the stress generated during the charge reaction is homogenized by the smooth diffusion of Li into the Si phase through the silicide phase, followed by the absorption of Li in the Si phase homogeneously. Consequently, we concluded that the ternary silicide/Si composite exhibited better cycle stability than the binary silicide/Si composite, based on the aforementioned results.

The above results were obtained using a gas deposition electrode, composed of only an active material. In this study, we evaluated the LIB anode performance of $Cr_xV_{1-x}Si_2$/Si using a slurry electrode consisting of active material, conductive agent and binder,

utilizing the $Cr_xV_{1-x}Si_2$/Si composite electrode in order to check its practicality as anode material of LIB. We also observed the change in metallographic structure of $Cr_xV_{1-x}Si_2$/Si following the charge-discharge cycles to clarify the mechanism of capacity reduction.

2.2 Experimental

2.2.1 Preparation of silicide/Si composite.

We prepared silicide/Si composites (silicide:Si=67:33 wt.%) based on the ratio of Cr to V in the silicide phase. The constituents of each silicide/Si composite are shown in Table 2-1. The composite was prepared by the roll quenching method. First, we melted Si and the additive elements (total weight=50 g) in a button arc furnace and produced Si alloy ingots. The current value during melting was between 100 A and 300 A, and the melting was conducted in an Ar atmosphere. Subsequently, the Si alloy ingot was melted at 1973 K in an induction furnace in the Ar atmosphere. Boron nitride crucible was employed for suppressing the reaction with molten alloy. The molten alloy was dropped on a copper roll rotating at 40 m/s. Thereafter, we quenched the molten Si alloy rapidly and prepared Si alloy ribbons with a thickness of approximately 20 μm. Figure 2-1 shows a photograph of the Si alloy ribbon. We prepared alloy powders (active materials) by hand milling and classified them as <25 μm of alloy ribbons.

The X-ray diffraction (XRD, Smart Lab, Rigaku) measurements of the active materials were performed at 40 kV and 135 mA using Co Kα radiation. To observe the structure of the composite ribbons, we placed the composite ribbons in a Bakelite resin as the thickness direction of the ribbon became the embedded surface and polished mechanically. We used diamond sprays of 9, 3, and 1 μm and an alumina suspension of 100 nm as abrasives. We decreased the size of the abrasives and polished them. The cross-sectional observation of the alloy ribbon was performed using a field emission scanning electron microscope (FE-SEM, SU6600, Hitachi High-Technologies Corporation). The accelerating voltage was 15 kV. The element mapping image of Si and of the additive element was obtained via field-emission electron probe microanalysis (FE-EPMA, JXA-8500F, JEOL, Co., Ltd.). The accelerating voltage and irradiation current were fixed at 15 kV and 50 nA, respectively.

Figure 2-1. Photograph of silicide/Si composite ribbon prepared by rapid quenching method.

Table 2-1. Contents of synthesized silicide/Si composites.

Sample name	Contents of silicide/Si composite (mass%)			Phase ratio (mass%)	
	Si	Cr	V	Silicide	Si
$CrSi_2$/Si	67.8	32.2	-	67	33
$Cr_{0.9}V_{0.1}Si_2$/Si	67.8	29.1	3.1		
$Cr_{0.5}V_{0.5}Si_2$/Si	68.0	16.2	15.8		
$Cr_{0.1}V_{0.9}Si_2$/Si	68.1	3.2	28.7		
VSi_2/Si	68.1	-	31.9		

2.2.2 Electrochemical characterization of the silicide/Si composite electrode.

The activate material (composite powder), conductive assistant (Ketjen black, CarbonEC600JD, LION SPECIALTY CHEMICALS CO., Ltd.), and binder (polyamic acid, DREAMBOND, I. S. T Corporation) were mixed in the ratios of 80:5:15 (mass%). A slurry was prepared by dilution using N-methyl-2-pyrrolidone (FUJIFILM Wako Pure

Chemical Corporation, Ltd.,). The slurry was coated on a SUS316L foil (thickness:20 μm) using the doctor blade technique. The coating thickness was 50 μm. Followed by coating, the electrode sheet was dried at 343 K. Next, it was roll-pressed to ensure a 30 μm thickness of the active material layer. The active material mass of electrodes were about 3.5±0.5 mg/cm^2. We punched the electrode (diameter:11 mm) onto the electrode sheet. The capacity of electrodes were approximately 4 mA h (capacity density : 4.2 mA h/cm^2). The electrodes were heated in vacuum at 573 K for 1 h to imidize the binder. The electrochemical characterization was performed in a coin cell assembly (2032 type). The working electrode was a silicide/Si composite, the separator was a glass fiber filter, and the counter electrode was a Li metal (thickness:1 mm, diameter:12 mm). 1M Lithium hexafluorophosphate ($LiPF_6$) dissolved in ethylene carbonate (EC):diethyl carbonate (DEC) (EC:DEC=1:1 vol.%) (Kishida Chemical Co., Ltd.) was used as the electrolyte. The cell assembly was performed in an open dry chamber (HWR-60AR, DAIKIN INDUSTRIES Ltd.), at a dew point below -70 °C. An electrochemical measurement system (TOSCAT3100, TOYO SYSTEM Co., LTD.) was used for a galvanostatic charge-discharge test. The initial capacity of the electrodes was measured under a constant current (0.03 A g (silicide/Si composite)$^{-1}$). The cycling properties were evaluated with a charge capacity limit of 800 mA h g (silicide/Si composite)$^{-1}$ at 298 K. The current density

was set to approximately 0.3 A g (silicide/Si composite)$^{-1}$, corresponding to a C-rate of 0.2 C, and potential range was between 0.002 and 1.000 V vs. Li^+/Li.

2.2.3 Measurement of hardness of the silicide phase.

We prepared an ingot in a button arc furnace and confirmed that these ingots consist of only silicide by XRD. The ingots were placed in Bakelite resin and mirror-polished via mechanical polishing. We used a micro-Vickers hardness tester (FM-800, FUTURE-TECH CORP.) to measure the hardness of each silicide phase. The measuring load was 100 g.

2.2.4 Calculation of average diameter of the silicide phase.

The average diameter of the silicide phase in the Si/silicide composite was measured to investigate the change in size of the silicide phase before and after the charge-discharge cycling test. The binarization process was performed on the cross-sectional SEM images of the Si/silicide composite electrode before charging and after the 50th cycle using an image processing software (MITANI CORPORATION, Winroof) to separate the Si phase and the silicide phase. We calculated the equivalent circle diameter by measuring the area and the number of silicide phases from the result of the image analysis. The same process

was performed for five images of each sample, and we considered the average diameter of the silicide phase to be the average value.

2.3 Results and Discussion

2.3.1 Characterization.

Figure 2-2 shows the XRD patterns of powders prepared from Cr, V, and Si. Additionally, Table 2-2 summarizes the corresponding lattice parameters. Binary $CrSi_2$/Si was confirmed from the Si and $CrSi_2$ peaks. All peaks of VSi_2/Si were also assigned to Si and VSi_2. The ternary composites were confirmed from the presence of Si peaks, similar to the binary silicide/Si composites (Figure 2-2 (a)). The silicide peaks of $CrSi_2$ shifted to lower angular values with the increase in the amount of V (Figure 2-2 (b)). In addition, the lattice constant along the a-axis increased (Table 2-2). These results indicate that some of the Cr atoms in $CrSi_2$ are substituted by V, where the radius of V is larger than that of Cr. Thus, we confirmed that the ternary silicide/Si composites prepared in this study were composed of Si and $Cr_{1-x}V_xSi_2$, as intended.

(a)

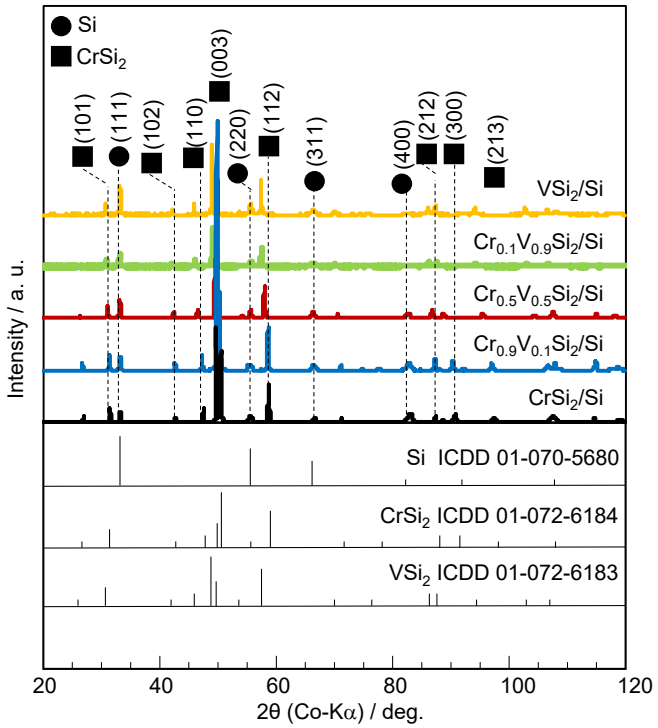

(b)

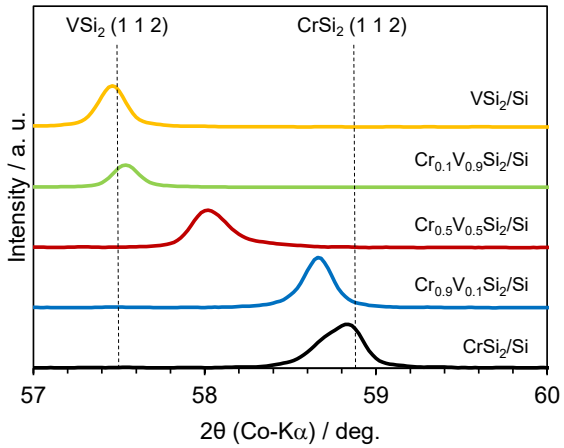

Figure 2-2. (a) XRD patterns of synthesized silicide/Si composites and (b) their enlarged view between 57° and 60°.

Table 2-2. Lattice constant of silicide phase in each silicide/Si composite.

Sample	Crystal structure of silicide	Lattice constant of silicide (Å)	
		a axis	*c* axis
$CrSi_2$/Si	Hexagonal	4.435	6.377
$Cr_{0.9}V_{0.1}Si_2$/Si		4.458	6.366
$Cr_{0.5}V_{0.5}Si_2$/Si		4.504	6.404
$Cr_{0.1}V_{0.9}Si_2$/Si		4.572	6.380
VSi_2/Si		4.579	6.384

The FE-EPMA results for $Cr_{0.1}V_{0.9}Si_2$/Si are shown in Figure 2-3. The white area of the SEM image (Figure 2-3 (a)) indicated Si, Cr, and V, and the concentrations of Cr and V in the white area were higher than those in the black area (Figure 2-3 (c), (d)). On the contrary, the black area mainly consisted of Si (Figure 2-3 (b)). These results support the conclusion that the white area is the silicide phase and the black area is the Si phase, as shown in Figure 2-3 (a). Figure 2-4 shows the cross-sectional SEM images of a composite ribbon. The structure of the prepared composites showed that the silicide phases were surrounded by the Si phases. Additionally, there were no significant differences in the shape and size of the silicide phase in any composite. Despite the variation in composition, the composite had similar structures. In addition, Figure 2-3 (a) shows that the Si phases and silicide phases are finely gathered together in the gray area. In addition, the entire cross-sectional SEM images of a composite ribbons are shown in Figure 2-5. When alloy ribbons are prepared by roll quenching, the structure of the side touched with roll during

quenching (roll side) is easier to become fine than that of the opposite side (free side) because cooling speed of roll side is faster than free side.[32,33] However, we could confirm no difference in the structure of the silicide/Si composite ribbons prepared in this study on each side. Figure 2-6 shows schematic diagram of roll quenching method and the relationship of roll side and free side as a reference.

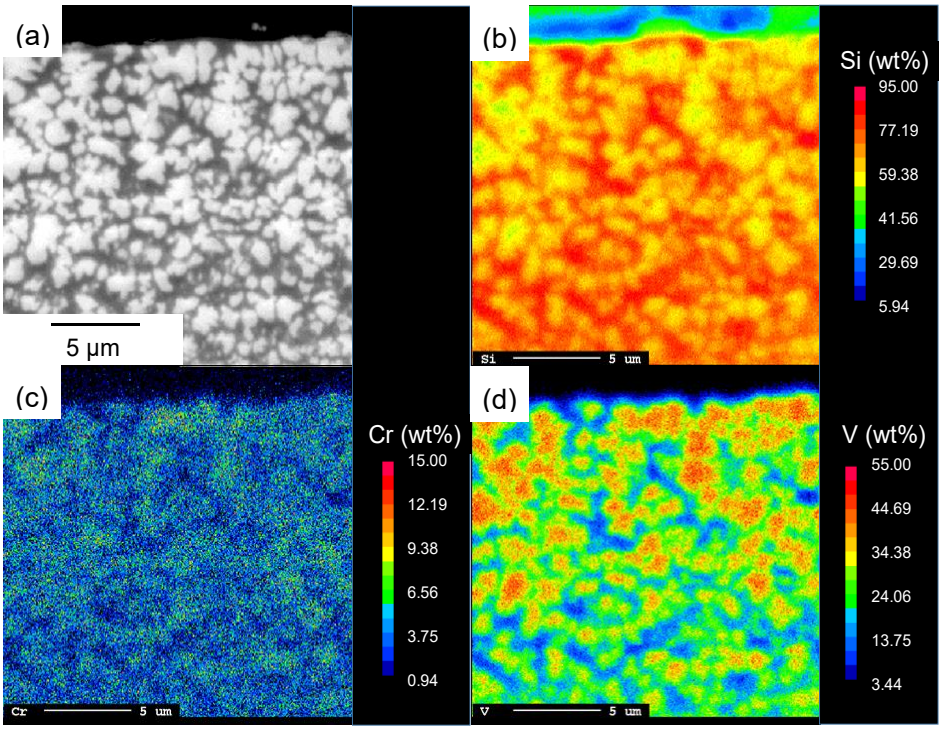

Figure 2-3. (a) SEM image of $Cr_{0.1}V_{0.9}$/Si and the corresponding FE-EPMA mapping of (b) Si, (c) Cr, and (d) V. The scale bar denotes 5 μm.

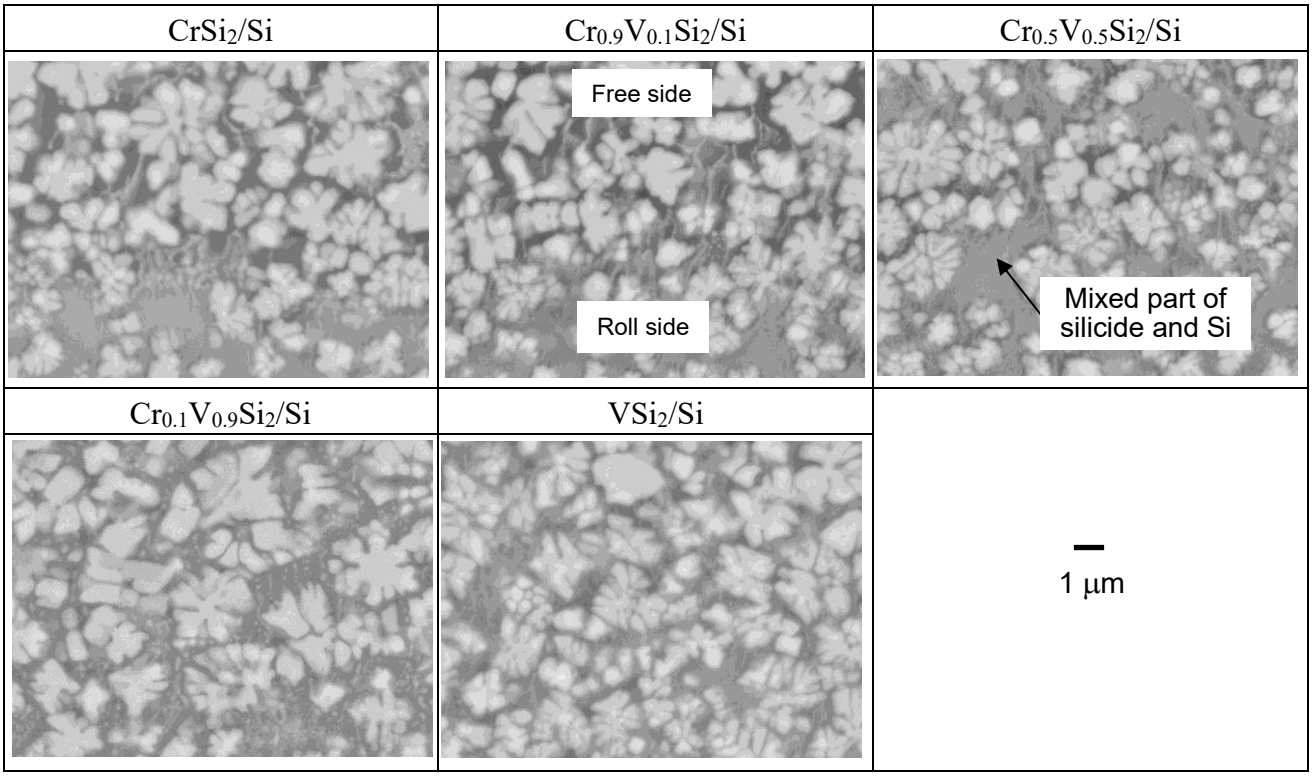

Figure 2-4. Cross-sectional SEM images of the prepared composites. The scale bar denotes 1 μm.

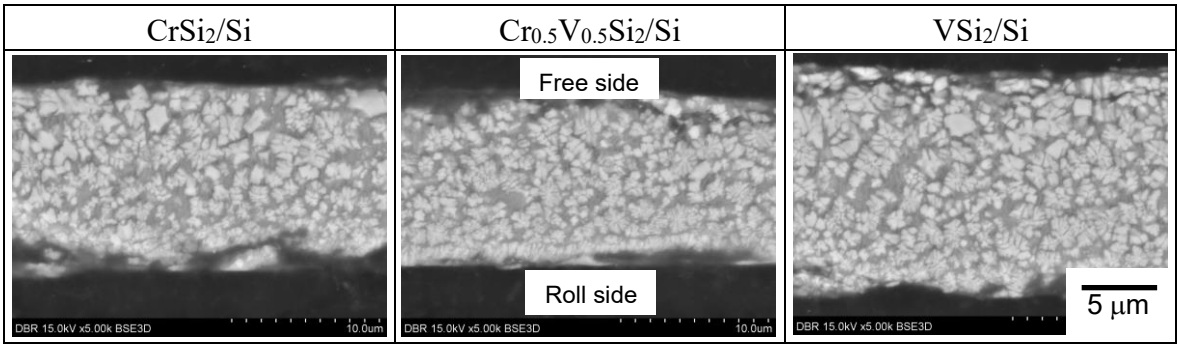

Figure 2-5. Entire cross-sectional SEM images of the prepared composites. The scale bar denotes 5 μm.

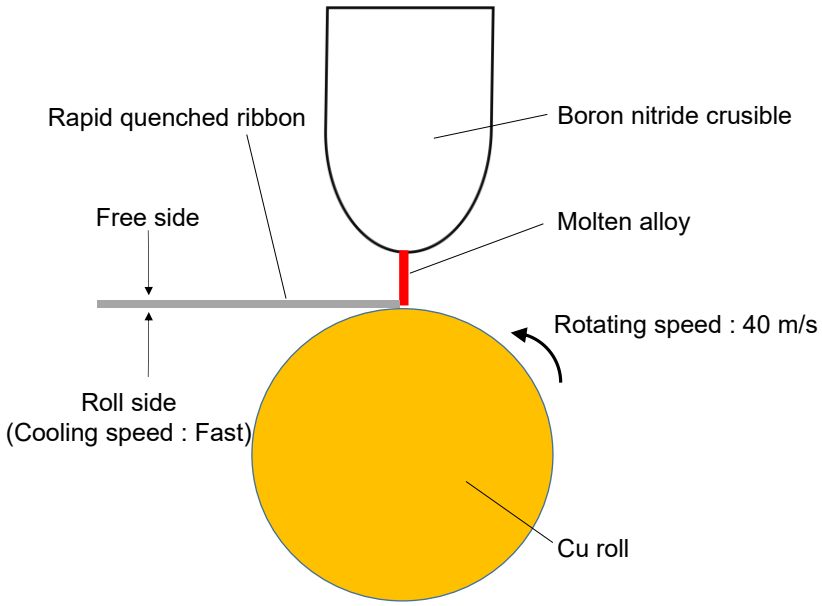

Figure 2-6. Schematic diagram of roll quenching method

2.3.2 Charge-discharge cycling test of the silicide/Si composite electrodes.

Figure 2-7 shows the initial charge-discharge curves of each silicide/Si composite electrodes. In the all electrodes, potential plateaus appeared in the charge (lithiation) reaction at around 0.1 V vs. Li/Li^+ and in the discharge (delithiation) reaction at approximately 0.45V vs. Li/Li^+. The plateaus are attributed to the alloying and dealloying reactions of Si and Li. We considered that the silicide phase in silicide/Si composite electrodes was not react with Li-ion because we have confirmed that only lithiation of Si in $FeSi_2$/Si electrode should occur while each $FeSi_2$- and Si-alone electrode reacted with Li.[34]

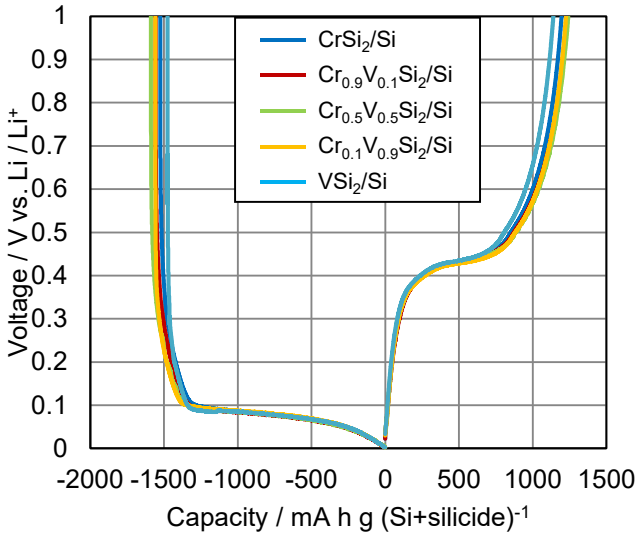

Figure 2-7. Initial charge-discharge curve of various silicide/Si composite electrodes in 1 M $LiPF_6$ in EC+DEC (EC:DEC=1:1 vol.%).

The initial charge and discharge capacity of the electrodes were almost the same. Additionally, there is little difference in the initial charge-discharge behavior among each silicide/Si composite electrode. Figure 2-8 shows cycle life of each silicide/Si composite electrode with a charge capacity limit of 800 mA h g (silicide/Si composite)$^{-1}$. In addition, coulombic efficiency are also exhibited in Figure 2-9. The $Cr_{0.9}V_{0.1}Si_2$/Si and $Cr_{0.5}V_{0.5}Si_2$/Si composite electrodes exhibited better cycle stabilities compared with $CrSi_2$/Si, owing to the addition of V. In particular $Cr_{0.5}V_{0.5}Si_2$/Si exhibited the best cycle stability. However, due to the increased amount of V in $Cr_{0.1}V_{0.9}Si_2$/Si and VSi_2/Si electrodes, they exhibited poor cycle stabilities and their coulombic efficiencies were decreased from the beginning of the cycle. It is considered that the decrease in the coulombic efficiency is caused by surface film formation on the new Si surface created by particle pulverization. We confirmed that $Cr_{0.5}V_{0.5}Si_2$/Si was a practically applicable composite electrode because it exhibited the best cycling performance as with the GD electrodes.

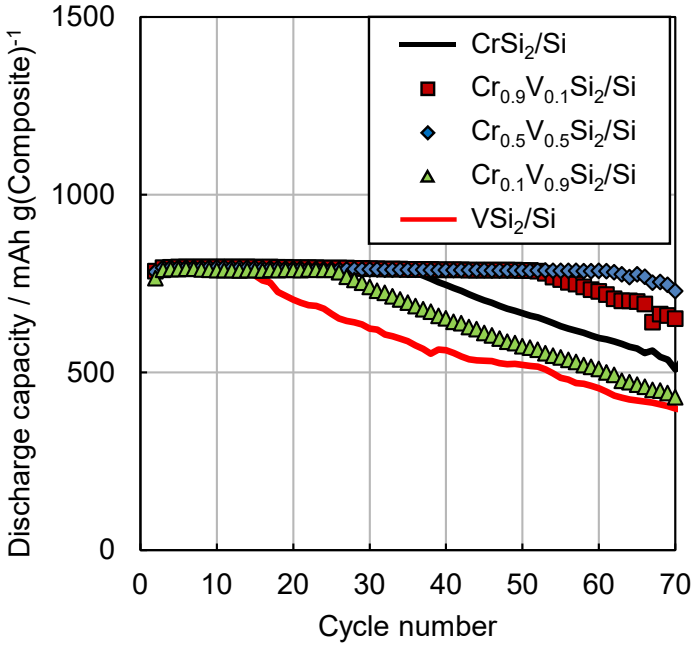

Figure 2-8. Cycle life of various silicide/Si composite electrodes in 1 M $LiPF_6$ EC/DEC (EC:DEC=1:1 vol.%).

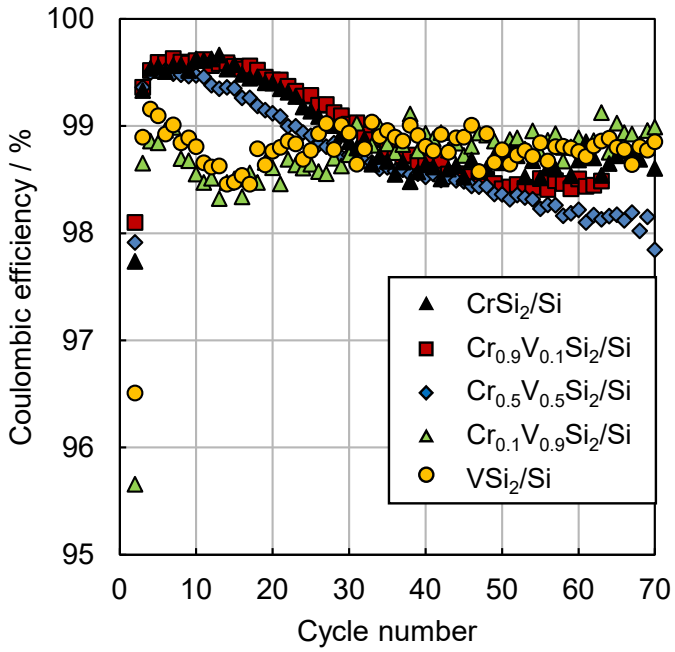

Figure 2-9. Coulombic efficiency of various silicide/Si composite electrodes in 1 M $LiPF_6$ EC/DEC (EC:DEC=1:1 vol.%) during charge-discharge test.

2.3.3 Cross-sectional observation of electrodes after charge–discharge.

Figure 2-10 shows the cross-sectional SEM images of $CrSi_2$/Si, $Cr_{0.5}V_{0.5}$/Si, and VSi_2/Si electrodes before and after the 50th charge–discharge. The highly magnified SEM images of the composite electrodes are also shown in Figure 2-11. In Figure 2-10, it was clear that the composite particles existed in the electrode after the 50th cycle; exfoliation of the composite particles from the current collector was not observed in any composite electrodes. In VSi_2/Si, the thickness of the electrode doubled and large cracks occurred in the electrode after the 50th cycle. The increase in the electrode thickness of both the $CrSi_2$/Si and $Cr_{0.5}V_{0.5}$/Si composites was approximately 1.5 times in each. In Figure 2-11, we observed that the silicide phase was pulverized and microcracks occurred in the composite particles after the charge–discharge cycles. The calculated average diameter results of the silicide phases before and after charge–discharge are shown in Table 2-3. After the 50th cycle, the silicide phases of all the composites became smaller he silicide phases of VSi_2/Si were significantly pulverized compared with those of $CrSi_2$/Si and $Cr_{0.5}V_{0.5}Si_2$/Si.

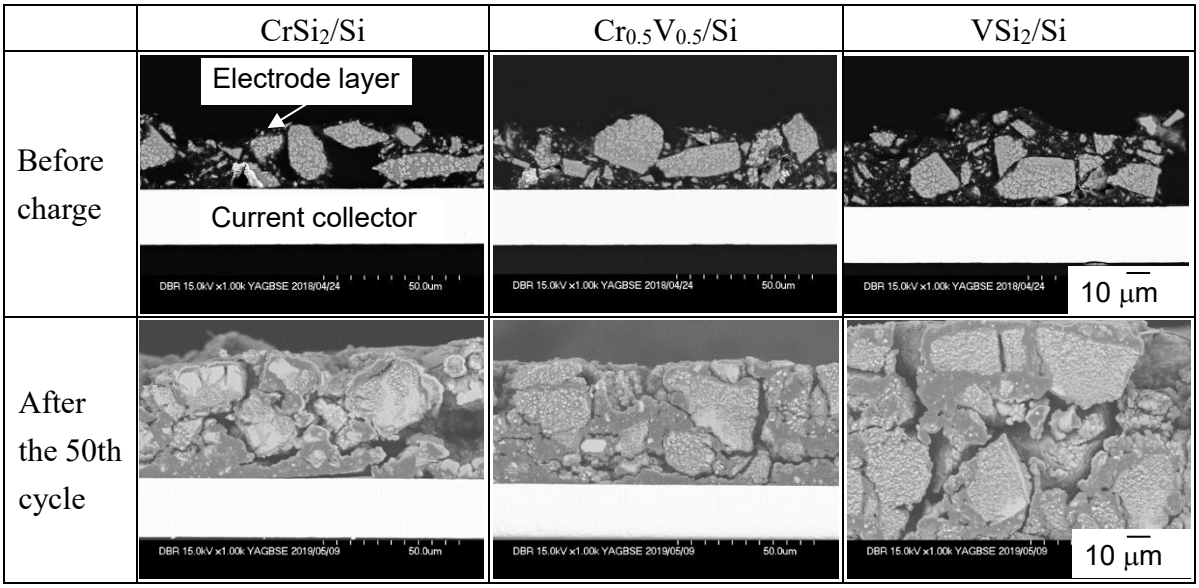

Figure 2-10. Cross-sectional SEM images of silicide/Si composite electrodes before and after the 50th cycle. The scale bar denotes 10 μm.

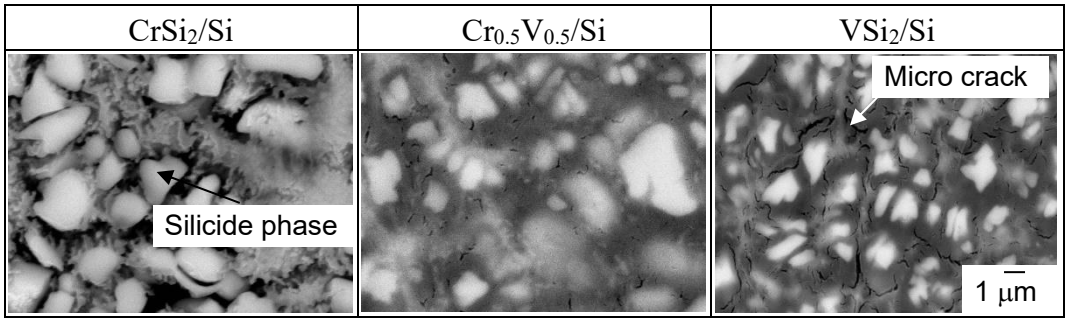

Figure 2-11. Cross section SEM images of silicide/Si composite electrodes after 50th cycle. The scale bar denotes 1 μm.

Table 2-3. Calculated average size of silicide phase before and after 50th cycle.

Sample	Average size of silicide phase (μm)	
	Before charge	After 50th cycle
$CrSi_2$/Si	3.0±0.2	2.3±0.5
$Cr_{0.5}V_{0.5}Si_2$/Si	3.2±0.2	1.4±0.3
VSi_2/Si	3.5±0.3	0.8±0.2

In the pulverizing silicide phase, the expansion of the composite particles becomes large owing to the cracks that occur in the particle in addition to the expansion of Li storage of the Si phase. As a result, the stress impressed on the entire electrode layer increases and the exfoliation at the interface between the active material and binder or collapse of the binder occurs. It is considered that the cycling stability of VSi_2/Si decreased because the electron conductive path or Li-ion conductive path was lost owing to the hard pulverization of the silicide phases. The coulombic efficiency of VSi_2/Si electrode reduced from the initial cycle, which indicated that the pulverization occurred from the initial cycle. The volume change of silicide during charge–discharge is small compared with Si because the amount of Li-ion storage of silicide is much smaller than that of Si.[9,35,36] Therefore, it is assumed that the silicide was transformed and cracked by the stress generated during the expansion of the Si phase. We measured the hardness of silicide, a parameter of deformability under the application of an external stress, to investigate the factors affecting the pulverization of silicide phases.

2.3.4 Relationship between hardness of silicide phase and cycle stability of silicide/Si composite.

Figure 2-12 shows the correlation between the Vickers hardness of silicides and the substituent constituents of the silicide phase. $CrSi_2$ exhibited the highest resistance to

pulverization after charge–discharge and was the hardest among all the evaluated silicides. In addition, the hardness of silicide decreased as the substitution amount of V increased with the addition of V to $CrSi_2$. There is a correlation between the hardness of the silicide phase and the resistance to pulverization of silicide during charge–discharge because the silicide phase pulverize with increase in the substitution amount of V, as shown in Table 2-3. When the hardness of silicide is increased, the silicide deformation due to the stress of Si expansion becomes smaller and it becomes difficult to pulverize the silicide. Hence, it is considered that the effect of prevention of crack occurrence and shape maintenance of composite particles can become greater. Based on the above results, it is suggested that compositing a silicide with high hardness and inhibiting pulverization of silicide is effective in improving the cycle stability of silicide/Si composites.

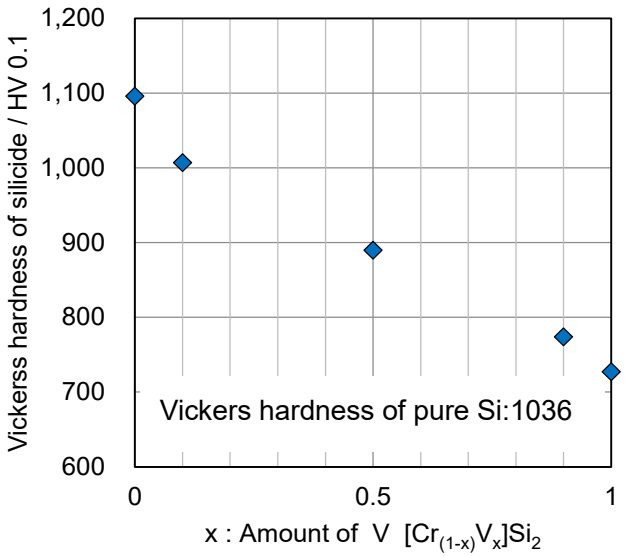

Figure 2-12. Correlation between Vickers hardness of silicides and x in $Cr_{1-x}V_xSi_2$.

In our previous studies, we have revealed that the addition of V to $CrSi_2$ improves the thermodynamic stability and spreads the crystal lattice of silicide. In addition, we have found that the charge repulsion between Li and the transition metal in $CrSi_2$ is smaller than that in case of VSi_2. We have reported that the diffusion of Li-ions in $Cr_{0.5}V_{0.5}Si_2$ was substantially improved by combining the effects of the small charge repulsion from $CrSi_2$ and the large crystal lattice of VSi_2. Besides the previous results, in this study we found that, although the hardness of $Cr_{0.5}V_{0.5}Si_2$ is smaller than that of $CrSi_2$, it is relatively high. Therefore, it is considered that it is difficult to pulverize $Cr_{0.5}V_{0.5}Si_2$/Si composite during charge–discharge and maintain the shape of the particles. Consequently, we revealed that hardness is an important mechanical property for compositing materials with Si, in addition to the elastic modulus that have been also measured in our previous

study. As shown in Figure 2-3 or 2-4, the silicide phases were surrounded by the Si phases in silicide/Si composite particles. It is inferred that in case of the structure above mentioned, the hardness of silicide is important because silicide is needed to not deform and maintain the shape of composite particles during Si expansion. Conversely, when the silicide phases surround the Si phases, the silicide phases relax the stress of Si expansion so, the elastic modulus of silicide is required.

2.4 Summary

The electrochemical performance of the $Cr_xV_{1-x}Si_2$/Si composite electrode was evaluated. The $Cr_{0.5}V_{0.5}Si_2$/ Si composite electrode exhibited the best cycling stability, similar to the GD electrode, and showed good practicality as an anode material for next generation lithium ion batteries. From the result of the cross-sectional SEM observation of the composite electrode following the cycling test, it was observed that silicide pulverization and the expansion of the $CrSi_2$/Si composite electrode after charge–discharge was suppressed. This is because $CrSi_2$ is difficult to deform during Si expansion owing to the hardness. It was concluded that the $Cr_{0.5}V_{0.5}Si_2$/Si composite electrode exhibited excellent cycling stability due to the prevention of silicide pulverization in $CrSi_2$ and the improvement of Li-ion diffusion owing to the substitution of V, as previously

reported. Additionally, when the structure of silicide/Si composite is that Si phases surround silicide phases, the hardness of silicide is important property for preventing the pulverization of composite during charge-discharge.

Chapter 3

Improved cycling performance of $Cr_xV_{1-x}Si_2$/Si composite electrode for application to lithium-ion battery anodes

3.1 Introduction

Because silicon (Si) exhibits ten times the theoretical capacity of graphite—currently the most widely used anode active material in lithium-ion batteries (LIBs)—substituting Si as the active material would greatly increase the LIB energy density. However, the formation of crystalline $Li_{15}Si_4$ during Si lithiation leads to a volumetric expansion of 380% per Si atom, which generates high stress.[6] Considerable strain accumulates during charge–discharge cycling, which collapses the electrode and pulverizes the Si particles. Consequently, Si-based electrodes exhibit poor cyclability. In addition, Si is brittle and exhibits high electrical resistivity and low Li^+ diffusion.

To overcome the disadvantages of Si-based electrodes, we synthesized various transition-metal silicide/Si composites and investigated their anodic properties. We have also reported that the silicide requires four key properties as follows[11-13,15-17,19,25,38-41]:

1. mechanical properties suitable for relaxation of the stress from Si

2. high electronic conductivity

3. moderate reactivity with Li^+

4. high thermodynamic stability.

Although all these properties must be fine-tuned to improve the electrochemical performance of silicide/Si composite electrodes, we adjusted the silicide properties and improved the electrochemical performance by compositing a ternary silicide because simultaneously adjusting all the binary silicide properties is difficult. As a result, the $LaNi_{0.1}Si_{1.9}$/Si composite electrode exhibited good cycling and superior high-rate performances compared to a $LaSi_2$/Si electrode.[20] We have also demonstrated that the $Cr_{0.5}V_{0.5}Si_2$/Si composite electrode showed considerably improved cycling stability compared with $CrSi_2$/Si and VSi_2/Si electrodes.[42,47] Because the Li diffusion in $Cr_{0.5}V_{0.5}Si_2$ is facilitated by combining the large crystal lattice of VSi_2 and the low charge repulsion between Si and Cr in $CrSi_2$ lattice, Li diffused into the Si through the $Cr_{0.5}V_{0.5}Si_2$ phase and homogeneously lithiated the Si. We have demonstrated that a composite electrode fabricated using a rigid silicide exhibited superior electrochemical performance when the composite formed a metallographic structure wherein the silicide phase was finely distributed in the Si one. Because $CrSi_2$ and $Cr_{0.5}V_{0.5}Si_2$ are harder than VSi_2, the silicide did not deform, which prevented the pulverization of the silicide/Si composite by the volumetric changes during charging–discharging. Consequently, the $Cr_{0.5}V_{0.5}Si_2$/Si

composite electrode exhibited an excellent cycling performance compared with a binary silicide/Si composite electrode.

It has been reported that the pulverization of Si during charge-discharge is prevented by refining the Si size. A lithium silicide (Li_xSi) phase initially forms on the Si particle surface during lithiation, and heterogeneously lithiated Si particles form a Li-rich phase, which locally generates a large heterogeneous volumetric change that propagates cracks and pulverizes Si particles—thereby disintegrating the entire electrode and degrading the electrode cycling performance.[48,49] Small Si particles homogeneously alloy with Li because Li can quickly diffuse throughout them. This means no stress is generated inside Si particles, which suppresses the Si-electrode failure. Xiao et al. have reported that Si particles smaller than 150 nm did not pulverize during Li absorption.[10] In addition, crystalline Si anisotropically expands because Li is stored along the Si <110> crystal direction.[50] Amorphous Si, on the other hand, homogeneously alloys with Li, thereby locally suppressing the formation of Li-rich phases. Therefore, amorphous Si particles are more robust than crystalline Si during charging and discharging. It has previously been shown that amorphous Si particles smaller than 870 nm do not pulverize.[51] Hence, many studies have improved electrode cycling performance by preparing Si nanostructures.[52-54]

Meanwhile, several other studies have shown that electrolyte additives such as vinylene carbonate (VC) and fluoroethylene carbonate (FEC) could improve the cycling stability of Si electrodes because the additives decomposed forming a stable film on the Si particle surface during the initial charging.[55-62] In this study, we applied mechanical grinding treatment (MG) with our $Cr_{0.5}V_{0.5}Si_2$/Si composite and refined the Si and silicide phases to enhance the electrode cyclability. Furthermore, the electrochemical performance of the electrodes was evaluated using an FEC-containing electrolyte. To clarify the effects of MG treatment and the addition of FEC to the electrolyte on the electrochemical performance, we observed the changes in the electrode structure and investigated the thickness and components of the film on the electrode surface after cycling.

3.2 Experimental

3.2.1 Preparation of silicide/Si composite by roll quenching

We prepared $Cr_{0.5}V_{0.5}Si_2$/Si composites ($Cr_{0.5}V_{0.5}Si_2$:Si = 67:33 wt.%) by roll quenching. Briefly, we weighed 8.1 g of Cr, 7.9 g of V, and 34.0 g of Si (total weight = 50 g). The weight ratios of Si, Cr, and V in the composite were 68.0, 16.2, and 15.8, respectively. They were melted in Ar in a button arc furnace to produce a Si–Cr–V alloy

ingot. The ingot was remelted at 1973 K in Ar in an induction furnace. The molten alloy was dropped onto a copper roll rotating at 40 m s^{-1} and was rapidly quenched to produce a ~20 μm-thick $Cr_{0.5}V_{0.5}Si_2$/Si composite ribbon.[41,47]

3.2.2 Mechanical grinding of $Cr_{0.5}V_{0.5}Si_2$/Si composite

The $Cr_{0.5}V_{0.5}Si_2$/Si composite ribbon was milled using a pestle and a mortar. The resulting composite particles were sieved to smaller than 100 μm. The powder (10 g) was put in a SUS304 vessel with 100 g, 9.5 mm diameter SUJ2 milling balls. The vessel was sealed under Ar. MG was carried out using a planetary ball mill (P-5, Fritsch) rotating at 300 rpm for 50 h. The particle size distribution of the prepared powder was measured in water using SALD-2300 (Shimadzu Corporation).

3.2.3 Characterization of $Cr_{0.5}V_{0.5}Si_2$/Si composite

The $Cr_{0.5}V_{0.5}Si_2$/Si composite was characterized using X-ray diffraction (XRD, SmartLab®, Rigaku) and Raman spectroscopy (NanofinderFLEX, Tokyo Instruments, Inc.). The XRD measurements were performed at 40 kV acceleration and using a 135 mA Co Kα irradiation current. The Raman spectra obtained from the $Cr_{0.5}V_{0.5}Si_2$/Si composites with and without MG by focusing the 532 nm (16.5 mW) line of a

neodymium-doped yttrium aluminum garnet (Nd:YAG) laser beam through a 50× objective lens.

To observe the composite structure, samples were encased in polyoxybenzylmethylenglycolanhydride (Bakelite) resin and were mechanically polished using successively smaller diamond sprays (9, 3, and 1 μm) and a 100 nm alumina suspension as abrasives. The prepared surfaces were observed using field-emission scanning electron microscopy (FE-SEM, SU6600, Hitachi High-Technologies Corporation) operating at 15 kV acceleration. The element mapping image of the $Cr_{0.5}V_{0.5}Si_2$/Si composite ribbon was obtained using field-emission electron probe microanalysis (FE-EPMA, JXA-8500F, JEOL, Co., Ltd.). The acceleration voltage and irradiation current were fixed at 15 kV and 50 nA, respectively.

3.2.4 Electrochemical characterization of $Cr_{0.5}V_{0.5}Si_2$/Si composite

We evaluated the electrochemical performance of the $Cr_{0.5}V_{0.5}Si_2$/Si composite, with and without MG as electrode active materials. The sample containing without MG powder was prepared by mortar milling the $Cr_{0.5}V_{0.5}Si_2$/Si composite ribbon and sieving under 25 μm. The powder sample with MG was also sieved under 25 μm. The activate material, conductive assistant (Ketjen black, CarbonEC600JD, Lion Specialty Chemicals Co., Ltd.),

and binder (polyamic acid, DREAMBOND, I. S. T. Corporation) were mixed in an 80:5:15 (mass%) ratio. *N*-methyl-2-pyrrolidone (FUJIFILM Wako Pure Chemical Corporation, Ltd.) was the slurry diluent. The slurry was coated on a 20 μm-thick SUS316L foil and dried at 343 K in air. The dried electrode sheet was roll-pressed. The pressed active material layer was 30 μm thick. The working electrode (diameter:11 mm) was punched from the electrode sheet and heated under vacuum at 573 K for 1 h to imidize the binder. A 2032-type coin cell was assembled in an open dry chamber (HWR-60AR, DAIKIN INDUSTRIES, Ltd.) at a dew point below −70°C. A glass filter (GA-100, Advantec Toyo Kaisha, Ltd.) and Li metal (1 mm-thick, 12 mm diameter) were used as the separator and counter electrode, respectively. The electrolyte was 1 mol dm^{-3} (M) lithium hexafluorophosphate ($LiPF_6$) dissolved in a mixture of ethylene carbonate (EC) and diethyl carbonate (DEC) (EC:DEC=1:1 vol.%) (Kishida Chemical Co., Ltd.) and was used with and without 3 vol.% FEC (Kishida Chemical Co., Ltd.). The initial charge–discharge behaviors were not changed in the electrolyte with or without additives (Figure 3-1 (a)). Additionally, FEC improved the cycle stability of $Cr_{0.5}V_{0.5}Si_2$/Si composite electrode than VC (Figure 3-1 (b)). Hence, we chose FEC as the film-forming additive to electrolyte. We cycled (charged and discharged) the cells using an electrochemical measurement system (TOSCAT3100, TOYO SYSTEM Co., Ltd.) at potentials between

0.002 and 1.000 V *vs*. Li^+/Li at 298 K. The initial electrode capacities were measured at a current density of 0.03 A g $(Si)^{-1}$. The current density during charging and discharging was set at 0.3 A g $(Si)^{-1}$, corresponding to a C-rate of 0.2*C* .In this study, 1*C* was defined as the current value that complete charging of the electrode measured initial capacity at a current density of 0.03 A g $(Si)^{-1}$ in one hour.

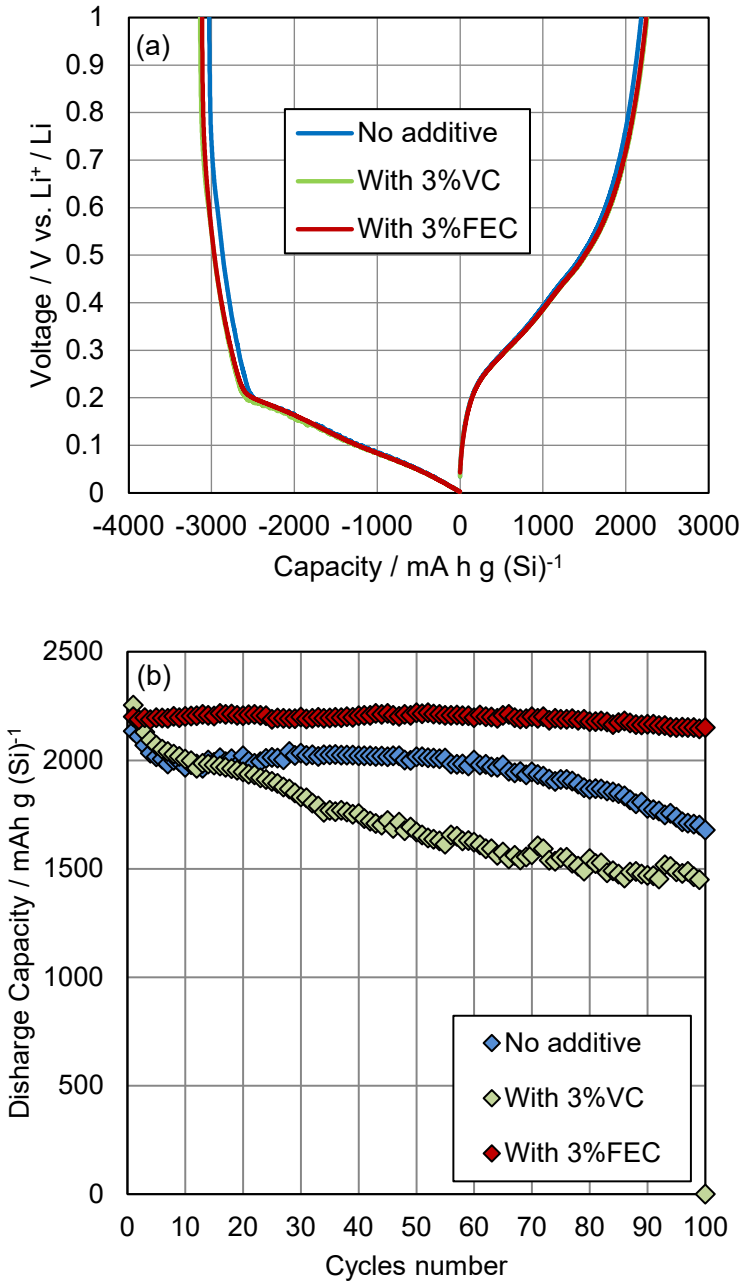

Figure 3-1. (a) Initial charge-discharge curve and (b) Cycling performance of $Cr_{0.5}V_{0.5}Si_2$/Si composite with MG electrode in 1 M $LiPF_6$ EC/DEC (EC:DEC=1:1, vol.%) no additive, with 3 vol.% VC, and with 3 vol.% FEC.

3.2.5 Analysis of films formed on cycled electrodes

Auger electron spectroscopy (AES, PHI710, ULVAC-PHI, Inc.) was used to analyze the thickness and composition of the films on the $Cr_{0.5}V_{0.5}Si_2$/Si composite surfaces. After 50 cycles, the coin cell was maintained at 2.0 V for 12 h to delithiate the composite electrode and was then disassembled in a glovebox to remove the working electrode. AES measurement of the electrode was carried out with Ar ion sputtering from surface of the electrode. The sputtering rate was approximately 7 nm min^{-1} (conversion value of SiO_2). The acceleration voltages of electron beam and ion gun were set at 3-5 kV and 2 kV, respectively. This measurement was performed at three points on each of the electrodes.

We measured the film Li and Si contents by solvent extraction. Briefly, a charged and discharged electrode was ultrasonicated in water for 30 min, and the water was filtered to remove the active material powder—leaving behind only the dissolved film components. The Li and Si contents of the aqueous extraction were measured using inductively coupled plasma–optical emission spectroscopy (ICP-OES, SPS-3500, Hitachi High-Tech Corporation). The other components dissolved in the water were analyzed using nuclear magnetic resonance (NMR, Avance III, 600 MHz, Bruker Corporation).

3.3 Results and discussion

3.3.1 Characterization of $Cr_{0.5}V_{0.5}Si_2$/Si composite

We investigated the effect of MG on the crystallinity of each phase in the $Cr_{0.5}V_{0.5}Si_2$/Si composite by XRD (Figure 3-2) and Raman spectroscopy (Figure 3-3). Si and silicide XRD peaks were observed for both samples (Figure 3-2 (a)). (Figure 3-2 (b)) shows that the Si (111) peak was only present in the XRD pattern for the sample without MG. The Si crystalline diameter calculated using Scherrer's formula was 450 nm. Furthermore, the Si phase was crystalline because a peak attributed to crystalline Si (*c*-Si) appeared at approximately 520 cm^{-1} (Figure 3-3)). In contrast, MG broadened the Si (111) peak (Figure 3-2 (b)), and a peak assigned to amorphous Si (*a*-Si) appeared in Figure 3-3; thus, MG changed *c*-Si into *a*-Si. The silicide phase in composite with and without MG samples exhibited crystalline peaks that shifted between those for VSi_2 and $CrSi_2$, thereby confirming a single ternary alloy (Figure 3-2 (c)). This ternary silicide ($Cr_xV_{1-x}Si_2$) was consisted by three element (Si, Cr and V) and formed by substituting some $CrSi_2$ Cr atoms with V ones, thereby shifting the peak toward VSi_2. We have reported the relationship between the amount of Cr substitution and the lattice parameter of $Cr_xV_{1-x}Si_2$ in Ref. 42. Moreover, MG broadened the silicide peak and shifted it to a higher angle. The calculated crystalline silicide size decreased from 800 nm (without MG)

to 10 nm (with MG). The peak shift suggested that MG generates lattice defects (vacancies), thereby reducing the $Cr_{0.5}V_{0.5}Si_2$ lattice constant. These results demonstrated that the $Cr_{0.5}V_{0.5}Si_2$/Si composite comprised Si and ternary silicide phases, Si became amorphous, and the silicide crystallite size decreased owing to MG.

Figure 3-4 shows particle size distributions of the $Cr_{0.5}V_{0.5}Si_2$/Si composite with and without MG. The d10, d50, and d90 values are summarized in Table 3-1. MG decreased the d50 particle size from 14 to 5.5 μm. Figure 3-5 shows the cross-sectional SEM images of the $Cr_{0.5}V_{0.5}Si_2$/Si composite ribbon, and the FE-EPMA results are shown in Figure 3-6. The SEM images (Figures 3-5 (a) and (b) and Figure 3-6 (a)) show two distinct phases in the composite without MG. The FE-EPMA results revealed that the dark regions are Si (Figure 3-6 (b)) and the bright regions are the $Cr_{0.5}V_{0.5}Si_2$ phase because only Si was detected in the dark regions, while and Cr and V were confirmed in the bright regions in addition to Si (Figures 3-6(c) and (d)). However, the Si and silicide phases were difficult to distinguish in the material that has been subjected to MG treatment because both phases consisted of finely dispersed nanoparticles (Figure 3-5 (c)). Therefore, the Si phase changed from crystalline to amorphous, and the silicide phase was finely crystallized and highly dispersed in the Si phase owing to MG.

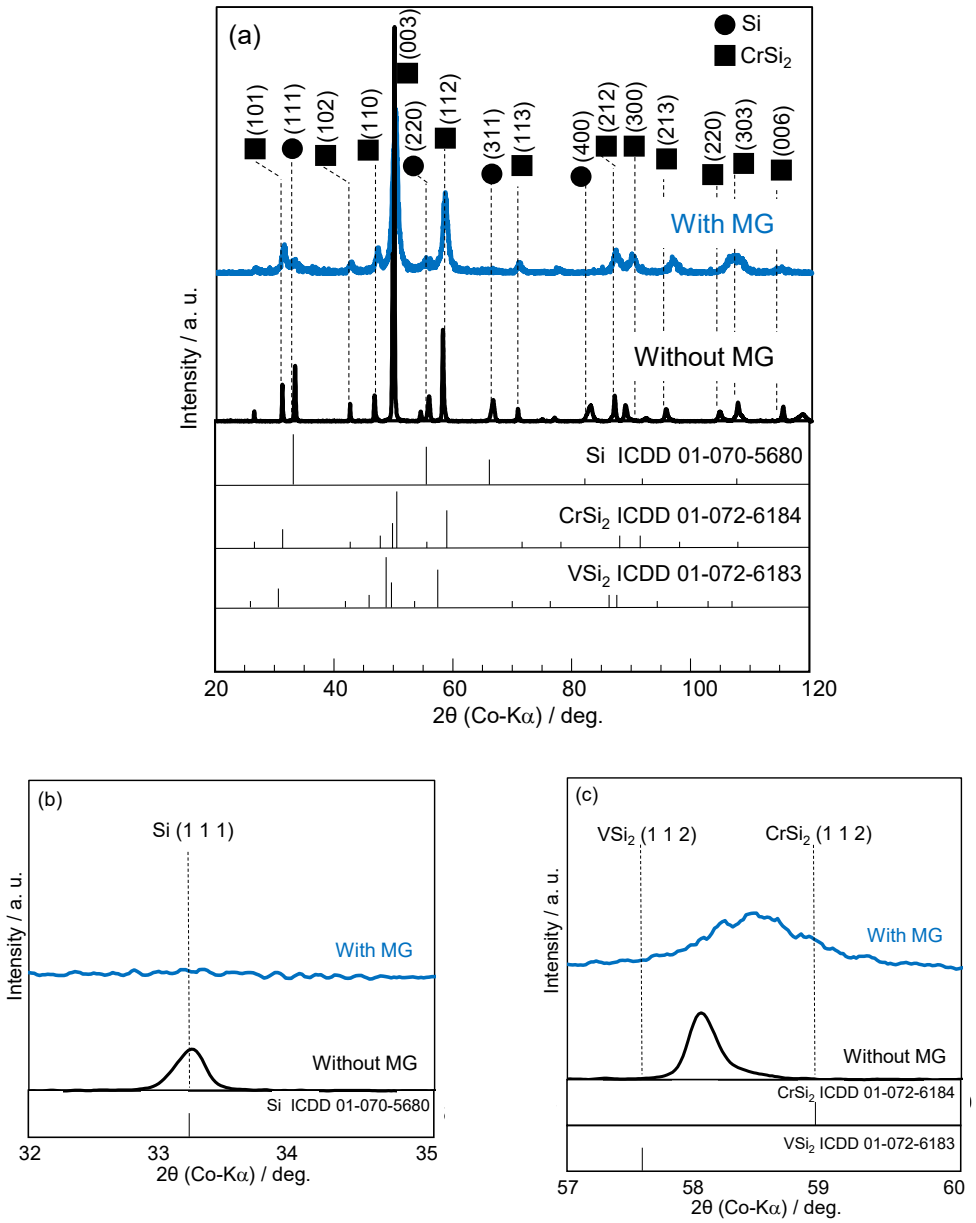

Figure 3-2. (a) XRD patterns of $Cr_{0.5}V_{0.5}Si_2$/Si composites with and without MG treatment and their enlarged view (b) between 32° and 35° and (c) between 57° and 60°.

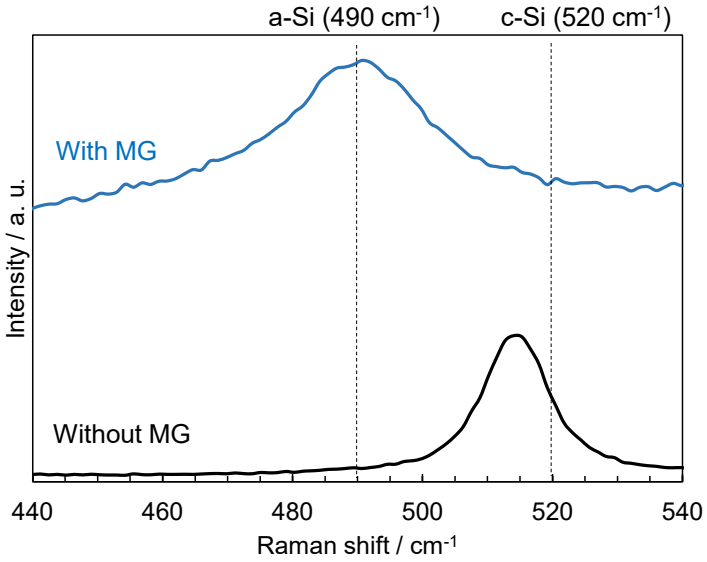

Figure 3-3. Raman spectra of $Cr_{0.5}V_{0.5}Si_2$/Si composite with and without MG process.

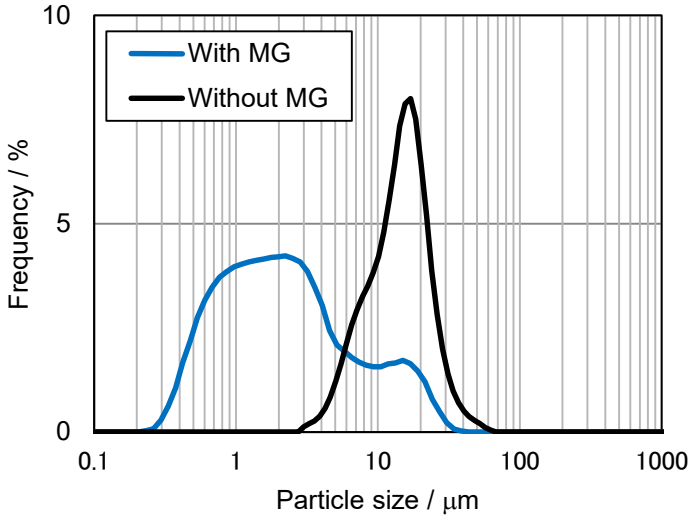

Figure 3-4. Particle size distribution of $Cr_{0.5}V_{0.5}Si_2$/Si composite with and without MG.

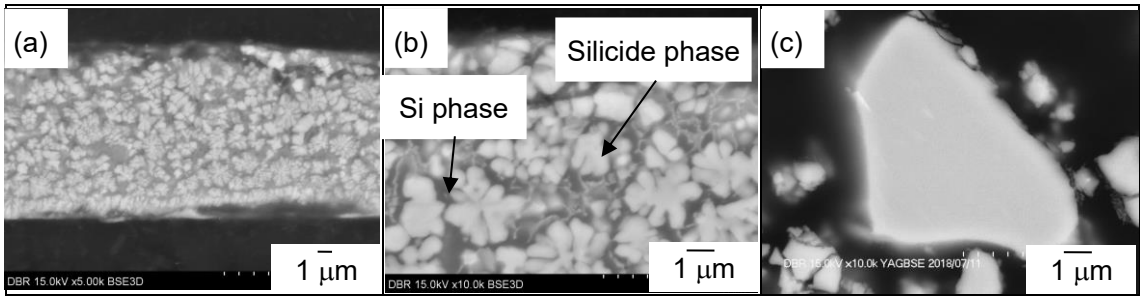

Figure 3-5. Cross-sectional SEM images of (a and b) $Cr_{0.5}V_{0.5}Si_2$/Si composite ribbon without MG and (c) the ribbon with MG. (a) presents entire image and (b and c) denote enlarged view. Scale bar: 1 μm.

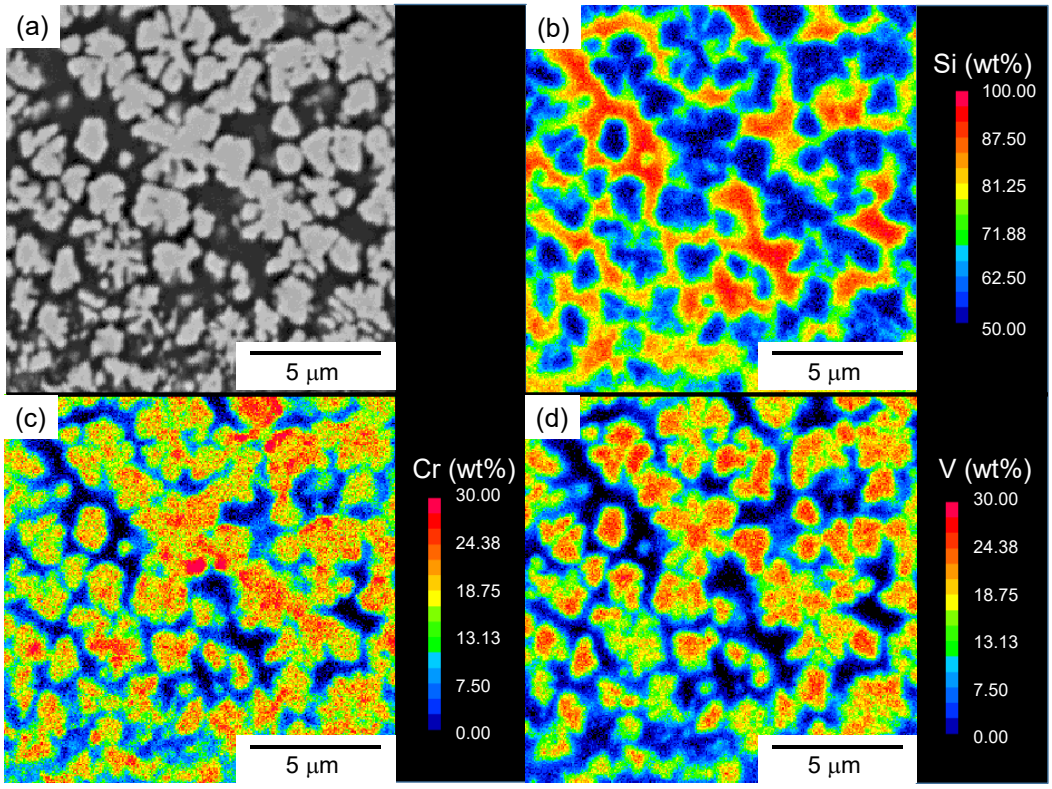

Figure 3-6. (a) SEM image of $Cr_{0.5}V_{0.5}Si_2$/Si composite ribbon without MG and the corresponding FE-EPMA maps of (b) Si, (c) Cr, and (d) V. Scale bar: 5 μm.

Table 3-1. Particle size of $Cr_{0.5}V_{0.5}Si_2$/Si composite with and without MG.

	Particle size (μm)		
	d10	d50	d90
Without MG	6.6	14.0	23.6
With MG	0.6	1.9	11.2

3.3.2 Charge–discharge cycling

Figure 3-7 displays the initial charge–discharge curves of the $Cr_{0.5}V_{0.5}Si_2$/Si composite electrodes in the FEC-free electrolyte. The electrode without MG exhibited potential plateaus at approximately 0.1 and 0.45 V *vs*. Li^+/Li in the charge and discharge curves, respectively. These plateaus are attributed to Si and Li alloying and dealloying. On the contrary, the potential plateaus of the electrode with MG increased and decreased to 0.2 and 0.2 V *vs*. Li^+/Li during charging and discharging, respectively. This change in behavior was attributed to the *a*-Si present in the MG treated material, as confirmed by Raman analysis (Figure 3-3). In addition, the initial charge–discharge curve of the $Cr_{0.5}V_{0.5}Si_2$/Si composite electrodes in the electrolyte with FEC shows in Figure 3-8. The charge–discharge behaviors were not changed in the electrolyte with and without FEC.

Table 3-2 shows the initial discharge capacity and the coulombic efficiency of the $Cr_{0.5}V_{0.5}Si_2$/Si composite electrodes. The initial comlombic efficiency was decreased by MG treatment. It was considered that irreversible reaction generated on particle surface

increased by MG treatment because the particle diameter became smaller (Figure 3-4). Initial discharge capacity and coulombic efficiency was not changed by adding FEC to the electrolyte. The decomposition of electrolyte at the beginning of the cycle preferentially could occur on the surface of the silicide phase because the electrical conductivity of silicide is higher than Si. The decomposition of FEC during charge-discharge had little influence on initial coulombic efficiency because the initial irreversible capacity derived form FEC decomposition was much smaller than that of the $Cr_{0.5}V_{0.5}Si_2$/Si composite. Hence, the initial coulombic efficiencies were not changed by adding FEC.

Figure 3-9 (a) shows the cycling performances of the $Cr_{0.5}V_{0.5}Si_2$/Si composite electrodes. For comparison, the cycling performance of the pure Si electrode is also shown. The reversible capacity of the pure Si electrode rapidly faded, whereas capacity degradation was suppressed in the $Cr_{0.5}V_{0.5}Si_2$/Si electrode without MG because Li had smoothly diffused into the Si phase, thereby homogenizing the stress generated during charging–discharging and suppressing the $Cr_{0.5}V_{0.5}Si_2$/Si composite particle pulverization, as previously reported by Domi et al.[42]

Table 3-3 summarizes the total amount of Li^+ alloyed with $Cr_{0.5}V_{0.5}Si_2$/Si composite and capacity retention of the $Cr_{0.5}V_{0.5}Si_2$/Si composite electrodes at the 100th cycle. Even

though the total amount of Li^+ alloyed with $Cr_{0.5}V_{0.5}Si_2$/Si composite with MG was larger than that without MG in the electrolyte without FEC, the capacity retention of the former considerably improved. In the electrolyte with FEC, we could confirm the same tendency. It was suggested that MG had formed *a*-Si and finely dispersed the silicide in the composite. The *c*-Si particles cracked and the electrode structure collapsed because *c*-Si had anisotropically expanded during charging. The *a*-Si, on the other hand, was homogeneously lithiated, which suppressed the electrode structural collapse because the Li-rich phases did not locally form.[51] In addition, the dispersal of the silicide phase with the Si on a nano-scale combines the beneficial properties of: relaxing stress in the Si, highly electron conductivity, and Li diffusivity in the entire electrode. For smaller active material particles, the short Li diffusion distance reduced the local stress, which suppressed electrode degradation during cycling.[10,63] Owing to these combined effects, the electrodes with MG electrodes exhibited superior cyclability.

Figure 3-9 (b) shows the cycle dependency of the $Cr_{0.5}V_{0.5}Si_2$/Si coulombic efficiency (CE). The electrode with MG exhibited higher CE than the electrode without MG, suggesting that particle pulverization in the electrode without MG had generated new surfaces and that the electrolyte irreversibly decomposed during charging and discharging. The suppression of particle pulverization in the MG treatment means that the electrolyte

did not decompose any further in each cycle, thereby preserving the CE.

The cycling performances of the electrode with and without MG in the FEC-containing electrolyte were both improved compared to the counterpart electrodes in the FEC-free electrolyte. Even in the FEC-containing electrolyte, the capacity of the electrode without MG still reduced with prolonged cycling, whereas the MG-treated electrode retained its capacity after 100 cycles and exhibited extremely good cycling stability. Additionally, the CE of the MG-treated electrode decreased after 50 cycles in the FEC-free electrolyte and remained low even after 100 cycles. Previous studies have reported that FEC decomposes at the beginning of cycling and forms a film on the Si electrode surface. The FEC-derived film suppresses the continuous electrolyte decomposition during charging and discharging cycles. These results demonstrated that FEC decomposition in the electrolyte also influences film formation on the surface of the $Cr_{0.5}V_{0.5}Si_2$/Si with MG electrode during cycling, as previously reported for other Si-based electrodes.[64-67] Therefore, MG markedly improved the $Cr_{0.5}V_{0.5}Si_2$/Si electrode cycling stability. Cross-sectional samples were analyzed after charge–discharge cycling to investigate the mechanism for the improved cyclability.

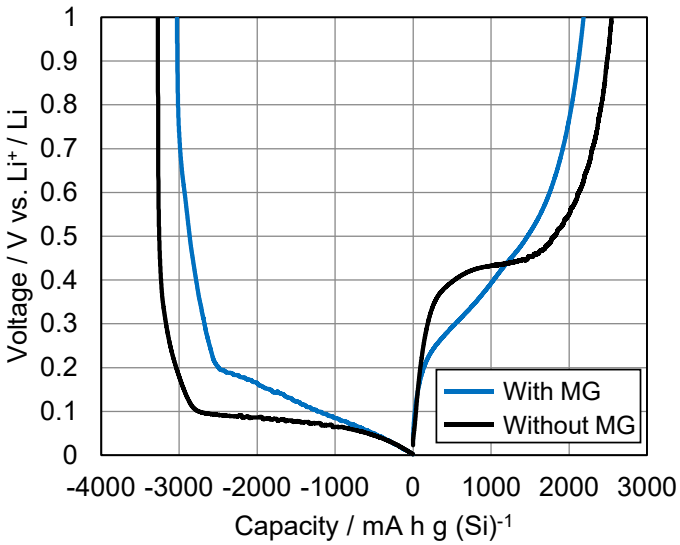

Figure 3-7. Initial charge-discharge curve of $Cr_{0.5}V_{0.5}Si_2$/Si composite with and without MG electrodes in 1 M $LiPF_6$ EC/DEC (EC:DEC=1:1, vol.%) in the absence of FEC.

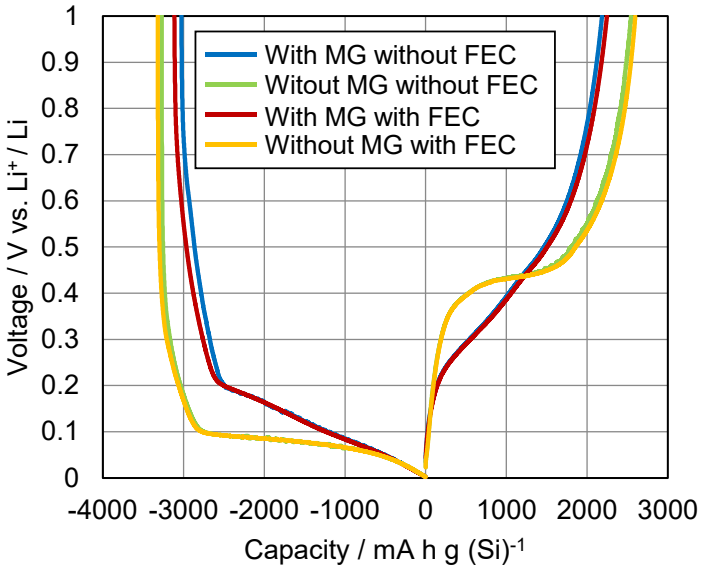

Figure 3-8. The first charge-discharge curves of $Cr_{0.5}V_{0.5}Si_2$/Si composite electrodes with and without MG in the electrolyte with and without FEC.

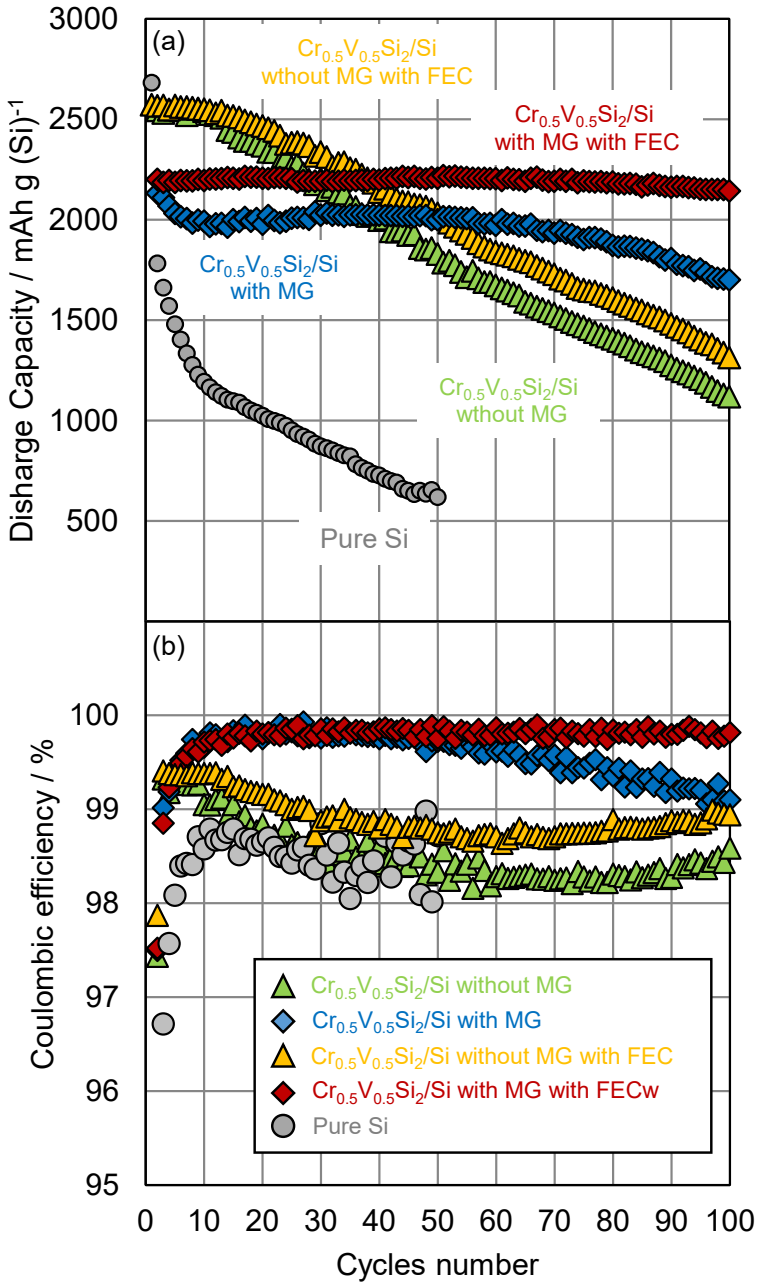

Figure 3-9. (a) Cycling performance and (b) Coulombic efficiency of $Cr_{0.5}V_{0.5}Si_2$/Si composite with and without MG and pure Si electrodes in 1 M $LiPF_6$ EC/DEC (EC:DEC=1:1, vol.%) without FEC and with 3 vol.% FEC.

Table 3-2. Initial discharge capacity and coulombic efficiency of the $Cr_{0.5}V_{0.5}Si_2$/Si composite electrodes.

	Initial discharge capacity (mA h g (Si)$^{-1}$)	Initial columbic efficiency (%)
Without MG without FEC	2545	78
With MG without FEC	2186	72
Without MG with FEC	2598	78
With MG with FEC	2247	72

Table 3-3. Total amount of Li^+ alloyed with $Cr_{0.5}V_{0.5}Si_2$/Si composite and capacity retention of the electrodes at the 100th cycle.

	Total amount of Li^+ (mol g (Si)$^{-1}$)	Capacity retention (%)
With MG without FEC	5.61×10^{-7}	79
Without MG without FEC	5.30×10^{-7}	43
With MG with FEC	6.31×10^{-7}	98
Without MG with FEC	5.76×10^{-7}	51

3.3.3 Cross-sectional observation of cycled electrodes

Figure 3-10 shows cross-sectional SEM images of the $Cr_{0.5}V_{0.5}Si_2$/Si electrode after the 50th cycle. The measured thicknesses of the active material layers are summarized in Table 3-4. The active material particles of the pure Si electrode were pulverized, and the electrode was approximately 3.5 times thicker after the 50th cycle. The $Cr_{0.5}V_{0.5}Si_2$/Si electrode without MG, on the other hand, was only 1.7 times thicker. Although the $Cr_{0.5}V_{0.5}Si_2$/Si electrode without MG exhibited higher total Li^+ storage than the pure Si one, the former thickened less because the formation of the Li-rich phase had been suppressed. In contrast, the thickness of the $Cr_{0.5}V_{0.5}Si_2$/Si electrode with MG negligibly changed after the 50th cycle. The magnified image shows that the pure Si particles clearly exhibited cracks and pulverization (Figure 3-10 (i)). Although the electrode of $Cr_{0.5}V_{0.5}Si_2$/Si without MG clearly exhibits cracked particles (Figure 3-10 (g)), it has fewer than the pure Si electrode. The $Cr_{0.5}V_{0.5}Si_2$/Si electrode with MG did not display any obvious particle cracking or pulverization (Figure 3-10 (h)). The $Cr_{0.5}V_{0.5}Si_2$/Si electrode with MG exhibited good cycling stability and high CE because the *a*-Si phase had homogenized Li storage and suppressed electrode damage during charging and discharging. The decrease in CE of the electrode without MG (Figure 3-9 (b)) because the electrolyte decomposition—wherein particle cracking forms a new electrode

surface—had been suppressed.

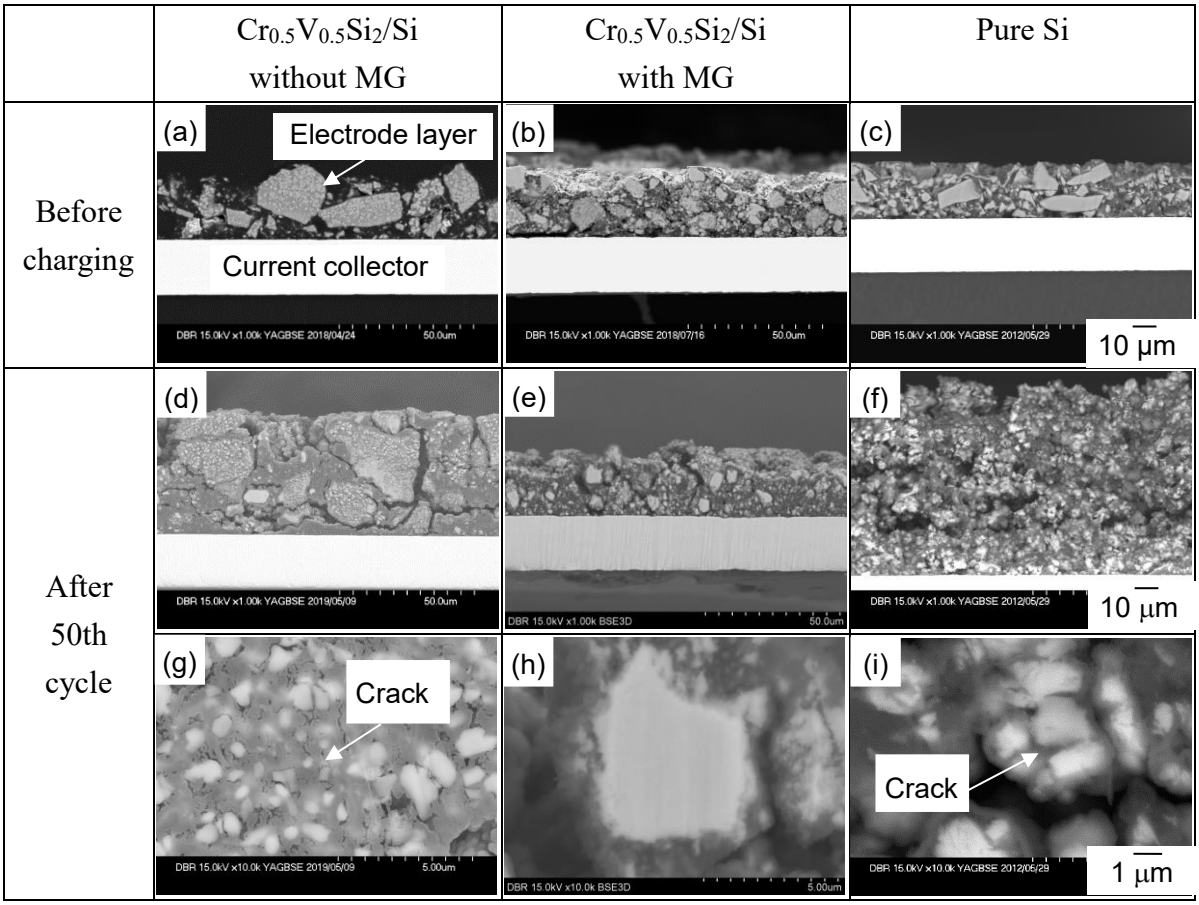

Figure 3-10. Cross-sectional SEM images of various electrodes (a-c) before and (d-i) after the 50th cycle (delithiation state) cycled in 1 M $LiPF_6$ EC/DEC (EC:DEC=1:1, vol.%) without FEC. Parts (a, d, and g) and (b, e, and h) denote the images of $Cr_{0.5}V_{0.5}Si_2$/Si composite electrode without MG and with MG, respectively. Parts (c, f, and i) present the images of pure Si electrode. The g, h, and i are high magnification images of d, e, and f, respectively. The scale bar denotes 10 μm (a-f) and 1 μm (g-i).

Table 3-4. Thickness of active material layer of $Cr_{0.5}V_{0.5}Si_2$/Si composite and pure Si electrodes before and after the 50th cycle (delithiation state) cycled in 1 M $LiPF_6$ EC/DEC (EC:DEC=1:1, vol.%) without FEC.

	Thickness of active material layer (μm)		
	$Cr_{0.5}V_{0.5}Si_2$/Si without MG	$Cr_{0.5}V_{0.5}Si_2$/Si with MG	Pure Si
Before charging	22±3	22±2	21±3
After 50th cycle	40±2	22±2	60±5

3.3.4 Analysis of thickness and components of film formed on electrode surface after charge–discharge cycling

Because the $Cr_{0.5}V_{0.5}Si_2$/Si electrode with MG retained its capacity after the 100th cycle in the FEC-containing electrolyte (Figure 3-9 (a)), we analyzed the thickness and composition of the film formed on the electrode surface after charge–discharge cycling to investigate the impact of the FEC on the cycling performance. The AES results of $Cr_{0.5}V_{0.5}Si_2$/Si composite electrode with MG after the 50th cycle are shown in Figure 3-11. The Si concentration increased with increasing detection depth from the electrode surface and was constant from a certain depth. The region that the Si concentration became constant from the electrode surface was attributed to the film which had formed during charge-discharge. The film was approximately 110 and 60 nm thick in the FEC-free and -containing electrolytes, respectively, revealing that the FEC had suppressed the film growth. Each electrode was analyzed at three points, and the film was uniformly thick at each point. Therefore, the film mainly consisted of Li, C, O, and Si regardless of

whether FEC had been added to the electrolyte, and the C and O were derived from the electrolyte solvent. The film on the $Cr_{0.5}V_{0.5}Si_2$/Si electrode surface consisted of lithium silicate, including Li and Si.

ICP analysis demonstrated that the film in the FEC-containing electrolyte contained more Li and Si than that in the FEC-free electrolyte (Figure 3-12). The FEC had decomposed and formed a film on the electrode surface at the beginning of cycling, and the film Li and Si contents increased after the 50th cycle. Although the film was thicker on the electrode in the FEC-free electrolyte than in the FEC-containing one, the former contained less Li after the 50th cycle (Figure 3-11). Moreover, the film Li and Si contents increased three and eight times from the 50th to the 100th cycles in the FEC-containing electrolyte, respectively; thus, the film had grown during cycling. In contrast, the film Li and Si contents increased only one-and-a-half times and remained constant from the 50th to the 100th cycles in the FEC-free electrolyte, respectively, suggesting that the FEC had suppressed further film growth.

Table 3-5 summarizes the NMR results for film components that dissolved from the $Cr_{0.5}V_{0.5}Si_2$/Si composite electrode with MG into the water. In the FEC-free electrolyte, the total H concentration was higher after the 100th cycle than after the 50th one. Because X–OCH_2HC_2O–Y and –OCH_2CH_3 were the EC- and DEC-derived decomposition

products, respectively, the solvent clearly had decomposed from the 50th to the 100th cycle in the FEC-free electrolyte. Adding FEC to the electrolyte suppressed the electrolyte decomposition because the H concentration did not increase. In addition, the LiF concentration was considerably higher in the FEC-containing electrolyte than in the FEC-free one. Previous studies have shown that a film containing FEC-decomposition-derived LiF forms on the electrode surface,[55-63] suggesting that the film thickened by electrolyte decomposition products continuously depositing on the electrode surface during cycling in the FEC-free electrolyte. This reduced the concentration of Si available to contribute to charging and discharging by forming a lithium silicate film and decreasing the capacity in the FEC-free electrolyte.

Therefore, adding FEC to the electrolyte suppresses the formation of the electrolyte-decomposition-derived film, thereby improving the cycling performance of the $Cr_{0.5}V_{0.5}Si_2$/Si composite electrode.

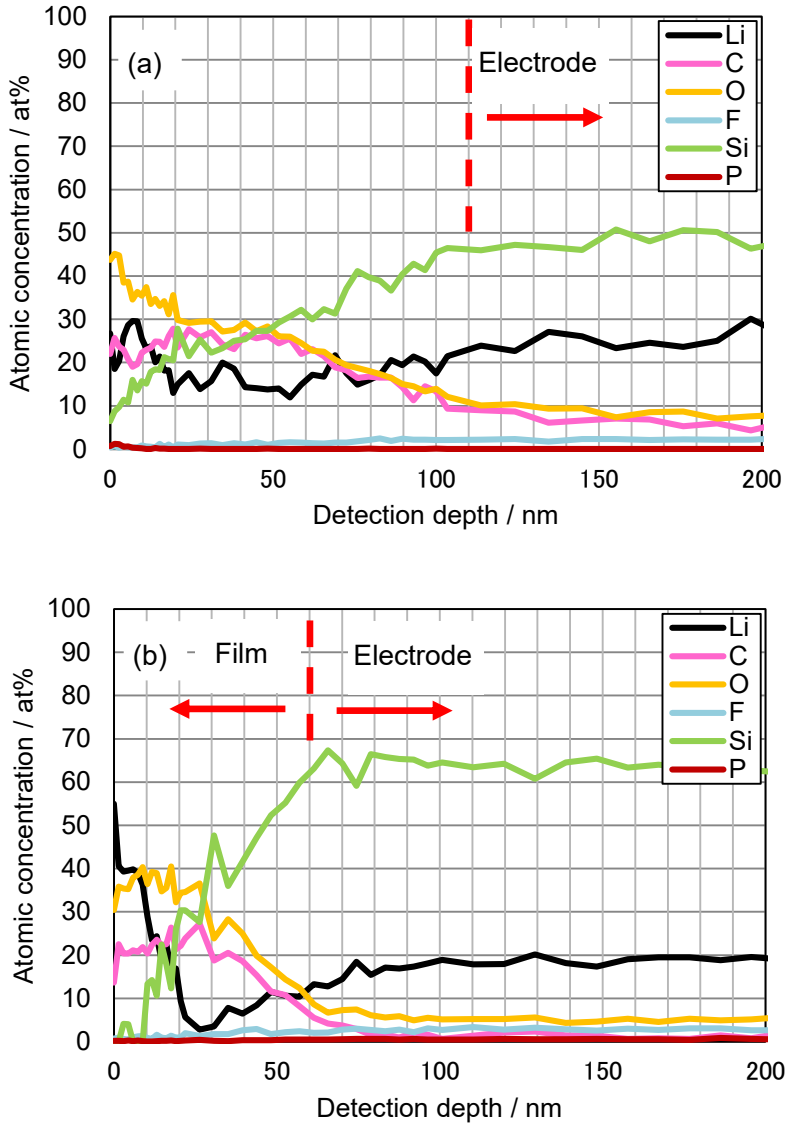

Figure 3-11. Results of AES of the $Cr_{0.5}V_{0.5}Si_2$/Si composite electrode with MG after the 50th cycle in 1 M $LiPF_6$ EC/DEC (EC:DEC=1:1, vol.%) (a) without FEC, (b) with 3 vol.% FEC.

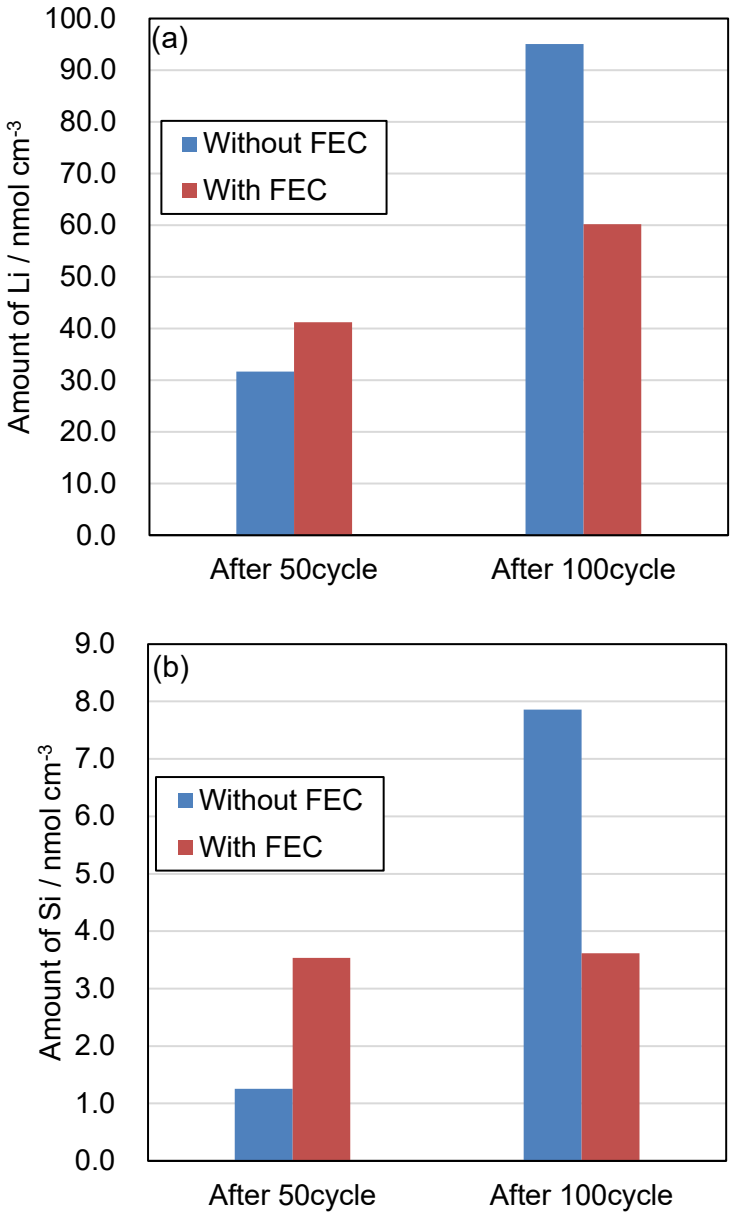

Figure 3-12. Amount of Li (a) and Si (b) included on surface film of the $Cr_{0.5}V_{0.5}Si_2$/Si composite electrode with MG after the 50th and the 100th cycles in 1 M $LiPF_6$ EC/DEC (EC:DEC=1:1, vol.%) without FEC and with 3 vol.% FEC. The amount was analyzed by ICP.

Table 3-3. NMR results of surface film on the $Cr_{0.5}V_{0.5}Si_2$/Si composite electrode (with MG) after the 50th and the 100th cycle in 1 M $LiPF_6$ EC/DEC (EC:DEC=1:1, vol.%) without FEC and with 3 vol.% FEC.

		H (nmol/cm^3)						LiF (nmol/cm^3)
		X-OCH_2HC_2O-Y	-OCH_3-	-OCH_2CH_3	$HCOO^-$	CH_3COO^-	Total H	
50th Cycle	Without FEC	9.02	0.13	4.40	0.11	0.95	22.00	0.25
	With FEC	4.40	0.01	1.32	0.31	0.66	11.00	2.04
100th Cycle	Without FEC	28.60	0.20	12.98	0.44	0.58	55.00	0.30
	With FEC	2.42	0.15	0.84	0.29	0.31	7.92	2.21

3.4 Summary

We investigated the electrochemical performances of $Cr_{0.5}V_{0.5}Si_2$/Si composite electrodes. MG improved the cyclability of the $Cr_{0.5}V_{0.5}Si_2$/Si composite electrodes by suppressing Si pulverization during charging and discharging because *a*-Si had homogeneously alloyed with Li. In addition, the $Cr_{0.5}V_{0.5}Si_2$ finely dispersed in the composite decreased the Si-lithiation-induced stress while achieving high electron conductivity and high Li diffusivity. The cycling performance of the $Cr_{0.5}V_{0.5}Si_2$/Si composite electrodes was further improved by adding FEC to the electrolyte. The FEC suppressed electrolyte decomposition during cycling, as indicated by suppressed film thickening and reduced lithium silicate formation. These results demonstrated that the cycling stability of silicide/Si composite electrodes could be improved by controlling the silicide/Si composite structure (i.e., *a*-Si formation or structural refinement) and by forming a suitable film to suppress electrolyte decomposition during charge–discharge cycling.

Concluding Remarks

In this thesis, the author tried to investigate new policy for improving properties of silicide/Si composite electrode and check its practicality as anode material of lithium-ion batteries.

1. The arrangements between Si and silicide phase in silicide/Si composite were controlled by rapid quenching for evaluating the influence of the positional relationship on the anode properties of LIBs. The electrode of Si-Zr and Si-Ti alloys which silicide phase formed around Si phase exhibited high initial capacity and good cycle stability. The collapse of Si-alloy was suppressed and the cycle stability was improved by selecting additive elements to locate the Si phase around the silicide phase.

2. The electrochemical performance of the $Cr_xV_{1-x}Si_2$/Si composite electrode was evaluated by using a slurry electrode in order to check its practicality as anode material of LIB. The $Cr_{0.5}V_{0.5}Si_2$/ Si composite electrode exhibited the best cycling stability, similar to the GD electrode, and showed good practicality as an anode material for next generation lithium ion batteries. It was revealed that silicide pulverization and the expansion of the $CrSi_2$/Si composite electrode after charge–discharge was suppressed.

This is because $CrSi_2$ is difficult to deform during Si expansion owing to the hardness. In addition to improve Li-ion diffusion, it was also important for improving cycle stability to prevent silicide pulverization. Moreover, when the structure of silicide/Si composite is that Si phases surround silicide phases, the hardness of silicide is important property for preventing the pulverization of composite during charge-discharge.

3. We evaluated the electrochemical performance of $Cr_{0.5}V_{0.5}Si_2$/Si composite electrode. The cyclabiity of $Cr_{0.5}V_{0.5}Si_2$/Si composite electrode was improved by mechanical grinding treatment. This reason was considered that the pulverization of $Cr_{0.5}V_{0.5}Si_2$/Si composite particle during charge-discharge was suppressed by forming amorphous Si and refining of the structure in silicide/Si composite. The cycle performance of $Cr_{0.5}V_{0.5}Si_2$/Si composite electrode was more improved by adding FEC. It was revealed that the film derived from decomposing FEC was formed by adding FEC. And the electrolyte decomposition as the cycle progresses was suppressed. From these results, it was effective for improving the cycle stability of silicide/Si composite electrode to control the structure of silicide/Si composite (formation of amorphous Si or structure refining) or suppress the electrolyte decomposition during charge-discharge cycles.

Acknowledgements

The author express sincere thanks to Professor Hiroki Sakaguchi at Department of Chemistry and Biotechnology, Graduated School of Engineering, Tottori University, for his passionate guidance, invaluable suggestions, and encouragement throughout his work.

The author would like to thanks Associate Professor Hiroyuki Usui for his appropriate suggestions, gentle coaching and helpful discussions.

The author is grateful to Associate Professor Yasuhiro Domi for his polite guidance, precise correction of the articles, and beneficial advices.

Special thanks to Eisuke Nakabayashi and all other members of the laboratory of Professor Hiroki Sakaguchi for supports of experiment and warmly welcome.

The author wish to thank Koichi Morii, Yuichiro Tago, and other collegues in Daido Steel Co., Ltd. for providing this opportunity, continuous guidance, and great supports.

Finally, the author gratefully thanks to my wife, Takako, my sons, Sota and Eita for always supporting in home.

References

[1] J. O. Besenhard, G. Eichinger, *Journal of Electroanalytical Chemistry and Interfacial Electrochemistry* **68** (1976) 1.

[2] G. Eichinger, J. O. Besenhard, *Journal of Electroanalytical Chemistry and Interfacial Electrochemistry* **72** (1976) 1.

[3] M.S. Whittingham, *Chem. Rev.* **104** (2004) 4271.

[4] J. B. Goodenough, Y. Kim, *Chem. Mater.* **22** (2010) 587 .

[5] C. J. Wen, R. A. Huggins, *J. Solid State Chem.* **37** (1981) 271.

[6] M. N. Obrovac, L. Christensen, *Electrochem. Solid-State Lett.* **7** (2004) A93.

[7] T. D. Hatchard, J. R Dahn, *J. Electrochem. Soc*. **151** (2004) A838.

[8] B. Key, R. Bhattacharyya, M. Morcrette, V. Seznec, J. M. Tarascon, and C. P. Grey, *J. Am. Chem. Soc.* **131** (2009) 9239.

[9] W. Wang, P. N. Kumta, *ACS Nano* **4** (2011) 2233.

[10] X. H. Liu, L. Zhong, S. Huang, S. X. Mao, T. Zhu, and J. Y. Huang, *ACS Nano* **6** (2012) 1522.

[11] H. Usui, Y. Kashiwa, T. Iida, and H. Sakaguchi, *J. Power Sources* **195** (2010) 3649.

[12] H. Usui, H. Nishinami, T. Iida, and H. Sakaguchi, *Electrochemistry* **78** (2010) 329.

[13] H. Usui, M. Shibata, K. Nakai, and H. Sakaguchi, *J. Power Sources* **196** (2011)

2143.

[14] H. Usui, N. Uchida, and H. Sakaguchi, *J. Power Sources* **196** (2011) 10244.

[15] H. Usui, N. Uchida, and H. Sakaguchi, *Electrochemistry* **80** (2012) 737.

[16] H. Sakaguchi, T. Iida, M. Itoh, N. Shibamura and T. Hirono, *IOP Conf. Ser. Mater. Sci.Eng.* **1** (2009) 012030.

[17] H. Usui, K. Maebara, K. Nakai, and H. Sakaguchi, *Int. J. Electrochem. Sci.* **6** (2011) 2246.

[18] H. Usui, M. Nomura, H. Nishino, M. Kusatsu, T. Murota, and H. Sakaguchi, *Matter. Lett.* **130** (2014) 61.

[19] H. Usui, K. Nouno, Y. Takemoto, K. Nakada, A. Ishii, and H. Sakaguchi, *J. Power Sources* **268** (2014) 848.

[20] Y. Domi, H. Usui, Y. Takemoto, K. Yamaguchi, and H. Sakaguchi, *J. Phys. Chem. C.* **120** (2016) 16333.

[21] H. Sakagichi, T. Toda, Y. Nagao, and T. Esaka, *Electrochem. Solid-State Lett*. **10** (2007) J146.

[22] H. Usui, Y. Kiri, and H. Sakaguchi, *Thin Solid Films* **520** (2012) 7006.

[23] B. Key, M. Morcrette, J. M. Tarascon, and C. P. Grey, *J. Am. Chem. Soc.* **123** (1976) 1196.

[24] K. Ogata, E. Salager, C. J. Kerr, A. E. Fraser, C. Ducati, A. J. Morris, S. Hofmann, and C. P. Grey, *Nat. Commun.* **5** (2014) article no. 4217.

[25] T. Iida, T. Hirono, N. Shibamura, and H. Sakaguchi, *Electrochem.* **76** (2008) 644.

[26] Y. Domi, H. Usui, Y. Takemoto, K. Yamaguchi, and H. Sakaguchi, *Chem. Lett*. **45** (2016) 1198.

[27] Y. NuLi, B. Wang, J. Yang, X. Yuan, and Z. Ma, *J. Power Sources* **153** (2006) 371.

[28] G. Xiao, H. Xue, G. Cheng, and X. Bao, *J. Chem. Eng. Chinese Universities* **20** (2006) 634.

[29] S. Kawakami, H. Kaidou, Y. Akita, H. Munakata, and K. Kanamura, *Electrochemistry* **83** (2015) 445.

[30] M. S. Bae, K. Y. Sohn, and W. W. Park, *Electronic Mat. Lett.* **10** (2014) 795.

[31] N. S. Nazer, R. V. Denys, H. F. Andersen, L. Arnberg, and V. A. Yartys, *J. Alloys Compd.* **718** (2017) 478.

[32] M. Armand, J. M. Tarascon, *Nature* **451** (2008) 652.

[33] M. N. Obrovac, L. J. Krause, *J. Electrochem. Soc.* **154** (2007) A103.

[34] J. W. Kim, J. H. Ryu, K. T. Lee, and M. Oh, *J. Power Sources* **147** (2005) 227.

[35] G. X. Wang, L. Sun, D. H. Bradhurst, S. Zhong, S. X. Dou, and H. K. Liu, *J. Alloys Compd.* **306** (2005) 249.

[36] M. S. Park, Y. J. Lee, S. Rajendran, M. S. Song, H. S. Kim, and J. Y. Lee, *Electrochim Acta* **50** (2005) 5561.

[37] W. R. Liu, N. L. Wu, D. T. Shieh, H. C. Wu, M. H. Yang, C. Korepp, J. O. Besenhard, and M. Winter, *J. Electrochem. Soc.* **154** (2007) A97.

[38] H. Usui, T. Kono, and H. Sakaguchi, *Int. J. Electrochem. Sci.* **7** (2017) 4322.

[39] H. Usui, K. Wasada, M. Shimizu, and H. Sakaguchi, *Electrochim. Acta* **111** (2013) 575.

[40] Y. Domi, H. Usui, H. Itoh, and H. Sakaguchi, *J. Alloys Compd.* **695** (2017) 2035.

[41] Y. Kimura, Y. Domi, H. Usui, and H. Sakaguchi, *Electrochemistry* **88** (2020) 330.

[42] Y. Domi, H. Usui, E. Nakabayashi, Y. Kimura, and H. Sakaguchi, *ACS Appl. Energy Mater.* **3** (2020) 7438.

[43] K. Takeshita, P. H. Shingu, *Trans. Japan Inst. Metals* **24** (1983) 529.

[44] S. Hong, Z. Xie, F. Dong, and D. Fei, D, *Physica B*. **405** (2010) 690.

[45] Y. Domi, H. Usui, Y. Shindo, S. Yodoya, H. Sato, K. Nishikawa, and H. Sakaguchi, *Electrochemistry* **88** (2020) 548.

[46] S. Du, S. N. Ellis, R. A. Dunlap, and M. N. Obrovac, *J. Electrochem. Soc.* **163** (2016) A13.

[47] Y. Kimura, Y. Domi, H. Usui, and H. Sakaguchi, *ACS Omega* **6** (2021) 8862.

[48] Y. Domi, H. Usui, A. Ando, K. Nishikawa, and H. Sakaguchi, *ACS Appl. Energy Mater.* **3** (2020) 8619.

[49] Y. Domi, H. Usui, K. Yamaguchi, S. Yodoya, and H. Sakaguchi, *ACS Appl. Mater. Interfaces* **11** (2019) 2950.

[50] S. W. Lee, M. T. McDowell, J. W. Choi, and Y. Cui, *Nano Lett.* **11** (2011) 3034.

[51] M. T. McDowell, S. W. Lee, J. T. Harris, B. A. Korgel, C. Wang, W. D. Nix, and Y. Cui, *Nano Lett.* **13** (2013) 758.

[52] H. Wu, Y. Cui, *Nano Today* **7** (2012) 414.

[53] M. T. McDowell, I. Ryu, S. W. Lee, C. Wang, W. D. Nix, and Y. Cui, *Adv. Mater*. **24** (2012) 6034.

[54] B. Liu, X. Wang, H. Chen, Z. Wang, D. Chen, Y.-B. Cheng, C. Zhou, and G. Shen, *Sci. Rep.* **3** (2013) 1622.

[55] I. A. Profotilova, C. Stock, A. Schmitz, S. Passerini, and M. Winter, *J. Power Sources* **222** (2013) 140.

[56] M.-Q. Li, M.-Z. Qu, X.-Y. He, and Z.-L. Yu, *Electrochim. Acta* **54** (2009) 4506.

[57] F. Maroni, R. Raccichini, A. Birrozzi, G. Carbonari, R. Tossici, F. Crone, R. Marassi, and F. Nobili, *J. Power Sources* **269** (2014) 873.

[58] Z. Jiang, C. Li, S. Hao, K. Zhu, and P. Zhang, *Electrochem. Acta* **115** (2014) 393.

[59] A. Bordrs, K. Emom, and T. F. Fuller, *J. Power Sources* **257** (2014) 163.

[60] V. Etacheri, O. Haik, Y. Goffer, G. A. Roberts, I. C. Stefan, R. Fasching, and D. Aurbach, *Langmuir* **28** (2012) 965.

[61] X. Wang, L. Sun, R. A. Susantyoko, and Y. Fan, Q. Zhang, *Nano Energy* **8** (2014) 71.

[62] Y. Domi, H. Usui, M. Shimizu, K. Miwa, and H. Sakaguchi, *Int. J. Electrochem. Sci.* **10** (2015) 9678.

[63] Y. Domi, H. Usui, K. Sugimoto, and H. Sakaguchi, *Energy Technology* **7** (2019) 1800946.

[64] N. S. Choi, K. H. Yew, K. Y. Lee, M. Sung, H. Kim, and S.-S. Kim, *J. Power Sources* **161** (2006) 1254.

[65] T. Jaumann, J. Balach, U. Langklotz, V. Sauchunk, M. Fritsch, A. Michaelis, V. Teltevskij, D. Mikhailova, S. Oswald, M. Klose, G. Stephani, R. Hauser, J. Eckert, and L. Giebeler. *Energy Storage Materials* **6** (2017) 26.

[66] K. Schroder, J. Alvarado, T. A. Yersak, J. Li, N. Dudney, L. J. Webb, Y. S. Meng, and K. Stevenson, *Chem. Mater.* **27** (2015) 5531.

[67] G. M. Veith, M. Doucet, R. L. Sacci, B. Vacaliuc, J. K. Baldwin, and F. Browning, *Scientific Reports* **7** (2017) 6326.

List of Publications

[1] Lithiation and Delithiation Properties of Silicide/Si Composite Alloy Electrodes Prepared by Rapid Quenching Method
Y. Kimura, Y. Domi, H. Usui and H. Sakaguchi,
Electrochemistry **88** (2020) 330.

[2] Anode Properties of $Cr_xV_{1-x}Si_2$/Si Composite Electrode for Lithium-ion Batteries
Y. Kimura, Y. Domi, H. Usui and H. Sakaguchi,
ACS Omega **6** (2021) 8862.

[3] Improved Cycling Performance of $Cr_xV_{1-x}Si_2$/Si Composite Electrode for Application to Lithium-ion Battery Anodes
Y. Kimura, Y. Domi, H. Usui and H. Sakaguchi,
Journal of The Electrochemical Society, in press.

Supplementary Publications

[1] Effect of Elemental Substitution on Electrochemical Performance of Silicide/Si Composite Electrodes for Litium-Ion Batteries
Y. Domi, H. Usui, E. Nakabayashi, Y. Kimura, and H. Sakaguchi,
ACS Appl. Energy Mater. **3** (2020) 7438.